ARTICLES
https://doi.org/10.1038/s41556-022-00846-7

nature cell biology

Reversible phase separation of HSF1 is required for an acute transcriptional response during heat shock

Hongchen Zhang[1,2,7], Shipeng Shao[3,7]✉, Yong Zeng[3], Xiaotian Wang[1,2], Yizhi Qin[1,2], Qiunan Ren[4], Shengqi Xiang[4], Yuxin Wang[5,6], Junyu Xiao[5,6] and Yujie Sun[1,2]✉

Heat-shock transcription factor 1 (HSF1) orchestrates the fast and vast cellular response to heat shock through increased expression of heat-shock proteins. However, how HSF1 rapidly and reversibly regulates transcriptional reprogramming remains poorly defined. Here by combining super-resolution imaging, in vitro reconstitution and high-throughput sequencing, we reveal that HSF1 forms small nuclear condensates via liquid–liquid phase separation at heat-shock-protein gene loci and enriches multiple transcription apparatuses through co-phase separation to promote the transcription of target genes. Furthermore, the phase-separation capability of HSF1 is fine-tuned through phosphorylation at specific sites within the regulatory domain. Last, we discovered that HSP70 disperses HSF1 condensates to attenuate transcription following the cessation of heat shock and further prevents the gel-like phase transition of HSF1 under extended heat-shock stress. Our work reveals an inducible and reversible phase-separation feedback mechanism for dynamic regulation of HSF1 activity to drive the transcriptional response and maintain protein homeostasis during acute stress.

As a conserved mechanism for various organisms to survive stress, the heat-shock (HS) response is vital for the maintenance of protein homeostasis. The central paradigm of the HS response involves the transcription of molecular chaperones that prevent protein misfolding and aggregation in response to elevated temperature and other stress triggers[1]. Heat-shock transcription factor 1 (HSF1) has been extensively studied due to its central role in regulating the HS response and restoring protein homeostasis. HSF1 orchestrates genome-wide transcriptional reprogramming to induce rapid and diverse changes in gene expression, resulting in the upregulation of several hundred genes and repression of several thousand genes[2]. In addition to acute stress, HSF1 regulates a wide range of targets in various chronic processes and non-stress conditions[3–5].

In contrast to malignant cancers, transcriptional activation during the HS response caused by acute stress is remarkably fast and vast, although HSF1 underlies the response in both cases[5]. The mechanism by which HSF1 promotes the remarkable transcriptional activation triggered by acute stress remains poorly understood. Decades of study have established a comprehensive understanding of the activation and attenuation cycle of HSF1 during HS[6]. However, the classic protein–DNA interaction-based model does not sufficiently explain the substantially different transcriptional responses caused by acute stress and in malignant cancers. Heat shock induces the formation of prominent subnuclear puncta known as nuclear stress granules/bodies (nSBs), which are commonly regarded as indicators of the HS response. However, studies have shown that nSBs are not associated with heat-shock-protein (HSP) genes in mammalian cells[7], in contrast to yeast[8]. Furthermore, a recent study reported that nSBs repress the transcription of HSP genes in human cells when the proteasome is inhibited[9]. Moreover, as rodent cells do not form nSBs but can still properly respond to HS[10], the canonical giant nSBs are unlikely to be the main driver of the drastic transcriptional activation of HSP genes during HS. Previous studies have identified many different post-translational modifications (PTMs) in the trimerization (leucine zipper 1–3, LZ1–3) and regulatory (RD) domains of HSF1 (refs. [11–14]), but the reason why nearby phosphorylation sites exhibit opposite effects on transcription activation remains a mystery.

Here we employed a suite of approaches and established a working model in which specific PTMs induced by HS regulate the formation of small HSF1 condensates on HSP gene loci, which recruit the transcription apparatuses and promote transcription. This finding provides a mechanistic explanation for the long-standing puzzle of how different phosphorylation sites regulate HSF1 transcription activity. In addition, we discovered that HSF1 activates target expression via different mechanisms in cells under acute stress and in malignant cells. Last, we demonstrate that HSP70 can disrupt the liquid–liquid phase separation (LLPS) of HSF1 and prevent the formation of a gel-like phase following prolonged HS. As the expression of HSP70 is activated by HSF1 during HS, this finding reveals an elegant negative-feedback mechanism that functions to attenuate HSF1 activity and restore cell homeostasis following HS. Together, our LLPS model for the dynamic regulation of HSF1 activity during HS provides a mechanistic explanation for large body of observations published over the last 40 years.

[1]State Key Laboratory of Membrane Biology, Biomedical Pioneering Innovation Center (BIOPIC), School of Life Sciences, Peking University, Beijing, China. [2]National Biomedical Imaging Center, College of Future Technology, Peking University, Beijing, China. [3]Beijing Institute of Heart Lung and Blood Vessel Disease, Beijing Anzhen Hospital, Capital Medical University, Beijing, China. [4]MOE Key Lab for Cellular Dynamics, School of Life Sciences, University of Science and Technology of China, Hefei, China. [5] State Key Laboratory of Protein and Plant Gene Research, Peking University, Beijing, China. [6]School of Life Sciences, Peking University, Beijing, China. [7]These authors contributed equally: Hongchen Zhang, Shipeng Shao. ✉e-mail: shaoshipengdq@163.com; sun_yujie@pku.edu.cn

Results

HSF1 forms condensates at both nSBs and HSP gene loci under HS. The role of LLPS in transcription regulation has been reported extensively in recent years[15–23]. Here, to explore whether LLPS plays a role in the regulation of HSF1, we first examined the amino-acid composition of human HSF1 using PONDR[24]. The HSF1 RD is highly enriched with low-complexity sequences (Extended Data Fig. 1a), suggesting that HSF1 may possess the capability to undergo LLPS. To explore this speculation, we transiently expressed enhanced green fluorescent protein (EGFP)-tagged HSF1 in HeLa cells and observed discrete granules in the nucleus after HS (Extended Data Fig. 1b), consistent with the formation of nSBs[7,25,26]. We further investigated the liquidity properties of these nSBs—that is, rapid induction, nearly round morphology, fast exchange, sensitivity to 1,6-hexanediol and responsiveness to blue light when fused to Cry2 (ref. [27]; Extended Data Fig. 1c–h). Using HSF1-knock-in cells (Extended Data Fig. 1i), we also demonstrated the formation of nSBs by endogenous HSF1 under HS (Fig. 1a). Nuclear stress granules/bodies are known to form through the direct binding of HSF1 to pericentromeric satellites[26,28]. To distinguish whether the nSBs were formed simply by the binding of HSF1 to satellites or facilitated by HSF1 LLPS, we quantified the fluorescence intensity in the bulk nucleus and nSBs (Fig. 1b). The fluorescence intensity of the nSBs increased with the total nuclear fluorescence intensity, indicating that more HSF1 molecules were recruited to the nSBs through protein–protein interactions, in addition to protein–DNA interactions. Using a LacI-HSF1 recruitment assay[22], we also found that intermolecular interactions play a role in driving the formation of HSF1 condensates during HS (Extended Data Fig. 1j,k). Together, these data demonstrate that HSF1 possesses the capability to undergo LLPS in living cells under HS.

As nSBs do not co-localize with HSF1-targeting genes during HS[7], we next investigated the distribution of HSF1 outside nSBs. After cells were subjected to HS and centrifugation of lysates, we found that nearly all HSF1 molecules were located in the precipitate (Fig. 1c), analogous to the stress-granule protein G3BP1. By contrast, proteins with a molecular weight similar to that of the HSF1 trimer[6] were found to be present in the supernatant, suggesting that all HSF1 molecules form protein condensates in HS cells. To gain a better understanding of the spatial organization of HSF1 in the nucleus, we performed stochastic optical reconstruction microscopy (STORM)[29], which allowed us to overcome the optical diffraction limit and resolve the localization of individual HSF1 molecules under HS conditions as well as in the absence of HS (NHS). We quantified the spatial distribution of HSF1 molecules and assessed their clustering behaviour. HSF1 molecules were dispersed in untreated cells, whereas small HSF1 puncta (diameter of approximately 300 nm) formed throughout the nucleoplasm of HS-treated cells (Fig. 1d). To determine whether such puncta were formed by HSF1 trimerization only or multivalent interactions, we performed STORM imaging on HS cells treated with 1,6-hexanediol. Compared with the HS-only cells, both the number of clusters and molecular density per cluster were dramatically reduced in the HS + 1,6-hexanediol treatment group (Fig. 1d–g), suggesting that multivalent interactions contributed to the formation of small HSF1 puncta. To determine whether the sensitivity of HSF1 puncta to 1,6-hexanediol originates from the disruption of protein–DNA interactions or a weak multivalent interaction, we performed electrophoretic mobility shift assays (EMSAs) using purified HSF1 and synthetic HS element (HSE) in 10% 1,6-hexanediol. We found that 1,6-hexanediol only disrupted weak and multivalent interactions between intrinsically disordered regions (IDRs) and did not affect the HSF1–DNA interactions (Extended Data Fig. 1l). Furthermore, the formation of small condensates could be observed in various cell lines, thus confirming multivalent interactions as a general mechanism of HSF1 clusters following HS (Extended Data Fig. 2a–f). We also used single-molecule tracking to measure the dynamics of HSF1 in living cells. Most HSF1 molecules were found to be freely diffused in cells in the NHS group. By contrast, HSF1 molecules were highly constrained in the HS-treated cells, which was consistent with their punctate state and suggested DNA binding (Extended Data Fig. 2g–j and Supplementary Video 1). Therefore, we investigated whether the small HSF1 condensates were in close spatial proximity to HSF1 target genes. We performed immunolabelling and fluorescence in situ hybridization (FISH) for HSF1 protein and several HSP genes (*DNAJB1*, *HSPA2* and *HSP90AA1*), followed by STORM imaging. These small HSF1 condensates frequently overlapped with DNA-FISH foci. There was less overlap between HSF1 puncta and *GAPDH*-gene foci, which is not a target of HSF1 (Fig. 1h–j). These results suggest that small HSF1 condensates are present at HSF1-target-gene foci through multivalent and weak interactions during HS.

HSF1 undergoes DNA binding-enhanced LLPS in vitro. Next, we investigated whether purified HSF1 can reconstitute LLPS in vitro. Interestingly, HSF1 purified from neither *Escherichia coli* nor HEK293F cells without HS could phase separate under a broad range of conditions (different salt concentrations, protein concentrations, pH and crowding reagents; Fig. 2a,b). By contrast, HSF1 purified from HS-treated HEK293F cells spontaneously formed micro-sized rounded droplets (Fig. 2b). The size of the HSF1 droplets increased with higher protein concentrations and lower salt concentrations (Fig. 2c–f). We then drew a phase diagram of HSF1 to illustrate that charge-mediated interactions might contribute to

Fig. 1 | HSF1 undergoes LLPS and forms small condensates during HS. a, Representative images of nSBs in HSF1-knock-in cells under NHS and HS (42 °C, 0.5 h) conditions. Scale bars, 10 μm. **b**, Left: schematic of HSF1 recruitment to nSBs in two scenarios. Right: analysis of the integrated nSBs (foci) and total nucleus intensities of cells transfected with HSF1–EGFP. Data are mean ± s.d.; error bands represent the s.e.m. of the smoothing line; $n = 2{,}256$ nSBs in 139 cells across three independent experiments. **c**, Western blot of HSF1 in the supernatant (S) and pellet (P) before and after HS (42 °C, 0.5 h). G3BP1 and HA–Cas9 were used as positive and negative controls, respectively. **d**, Super-resolution images of HSF1 under NHS, HS (42 °C, 0.5 h) and HS + 10% 1,6-hexanediol (Hex; 1 min) conditions. Magnified views of the regions in the yellow squares are shown (bottom). Top right: one nSB in HS cell magnified to show details. Scale bars, 5 μm; color legends in the magnified views indicate molecular density (arbitrary units). **e**–**g**, Cluster analysis of HSF1 molecules under NHS, HS and HS + Hex treatments. The cluster size (**e**), localization (**f**) and number (**g**) are shown. **f**, In box plots, boxes show the 25th to the 75th percentile with the median, and whiskers indicate 1.5× the interquartile range. **g**, Individual data points correspond to the average of a cell. Data are mean ± s.d. **f**,**g**, $n = 9$ (NHS), 11 (HS) and 10 (HS + Hex) cells pooled from three independent experiments. **h**, Super-resolution images of HSF1 condensates and FISH of HSF1 target genes under NHS and HS (42 °C, 0.5 h) conditions. *GAPDH* was used as a control. Insets: magnified views of the regions in the white boxes. Scale bars, 5 μm (main images) and 100 nm (insets). **i**, Percentage of cells with HSF1 condensates overlapping with HSP genes; $n = 35$ and 21 (*GAPDH*), 5 and 26 (*HSPA2*), 46 and 26 (*DNAJB1*), and 63 and 27 (*HSP90AA1*) foci and cells, respectively, from three independent experiments. **j**, Pearson's correlation of HSF1 and FISH over a 100 × 100 nm² region centred around the FISH signal under NHS and HS conditions. Data are mean ± s.d. HS, $n = 35$ and 21 (*GAPDH*), 57 and 26 (*HSPA2*), 46 and 26 (*DNAJB1*), and 63 and 27 (*HSP90AA1*) foci and cells, respectively, from three independent experiments; NHS, 31 and 16 (*GAPDH*), 42 and 19 (*HSPA2*), 42 and 20 (*DNAJB1*), and 39 and 20 (*HSP90AA1*) foci and cells, respectively, from three independent experiments. **f**,**g**,**j**, *P* values were determined using a paired two-tailed Student's *t*-test. Significant differences are labelled; $^{****}P < 0.0001$, $^{***}P < 0.001$, $^{**}P < 0.01$, $^{*}P < 0.05$; NS, not significant. **a**,**c**,**d**,**h**, Images are representative of three independent experiments.

HSF1 LLPS (Fig. 2g). Using the HaloTag knock-in cells, we estimated the concentration of endogenous HSF1 to be about 0.4 μM (Extended Data Fig. 3a–d). Accordingly, purified HSF1 alone could form droplets at concentrations below 0.4 μM (Fig. 2g). These results revealed an intrinsic capacity of HSF1 to phase separate at physiological concentration.

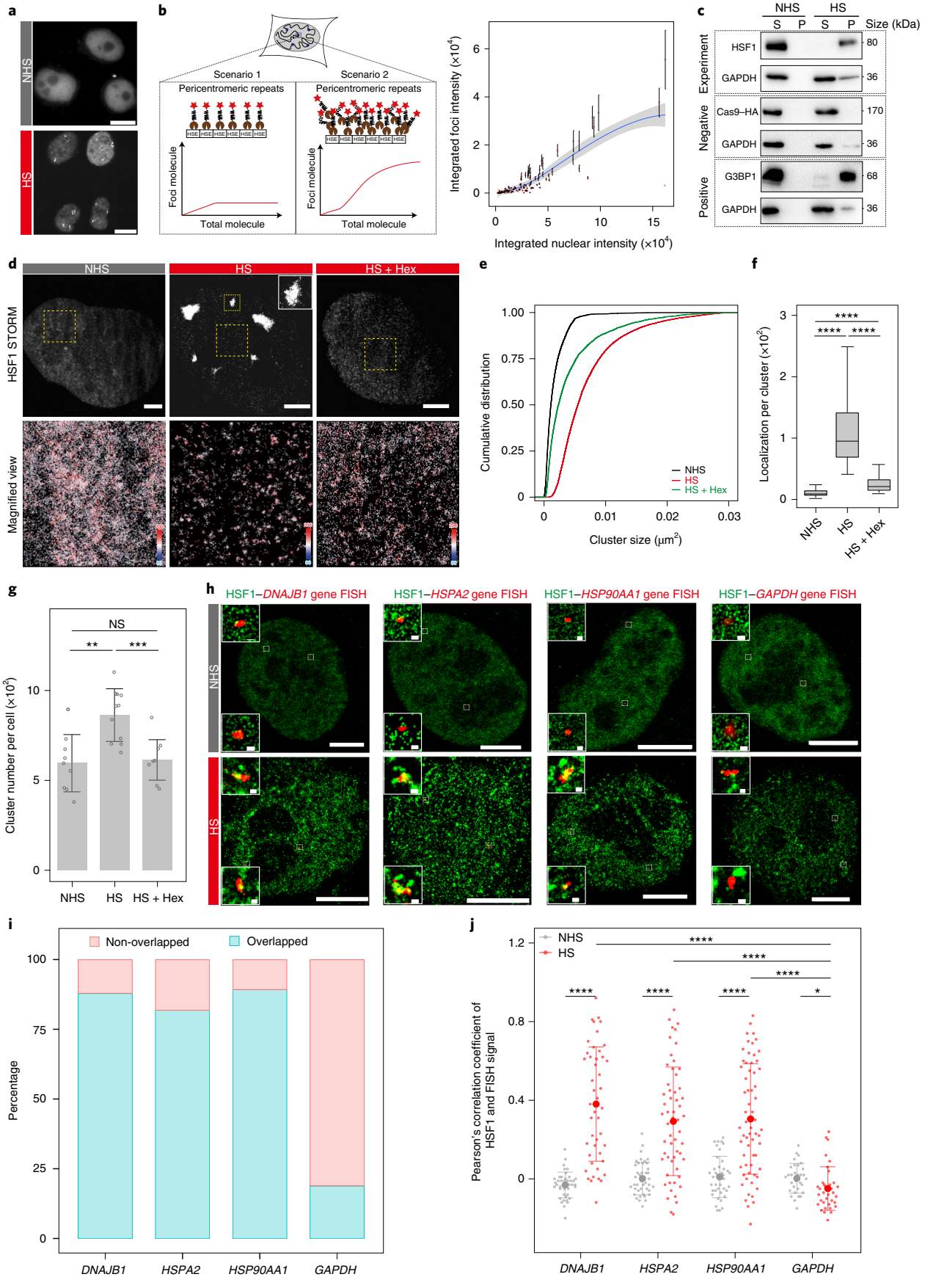

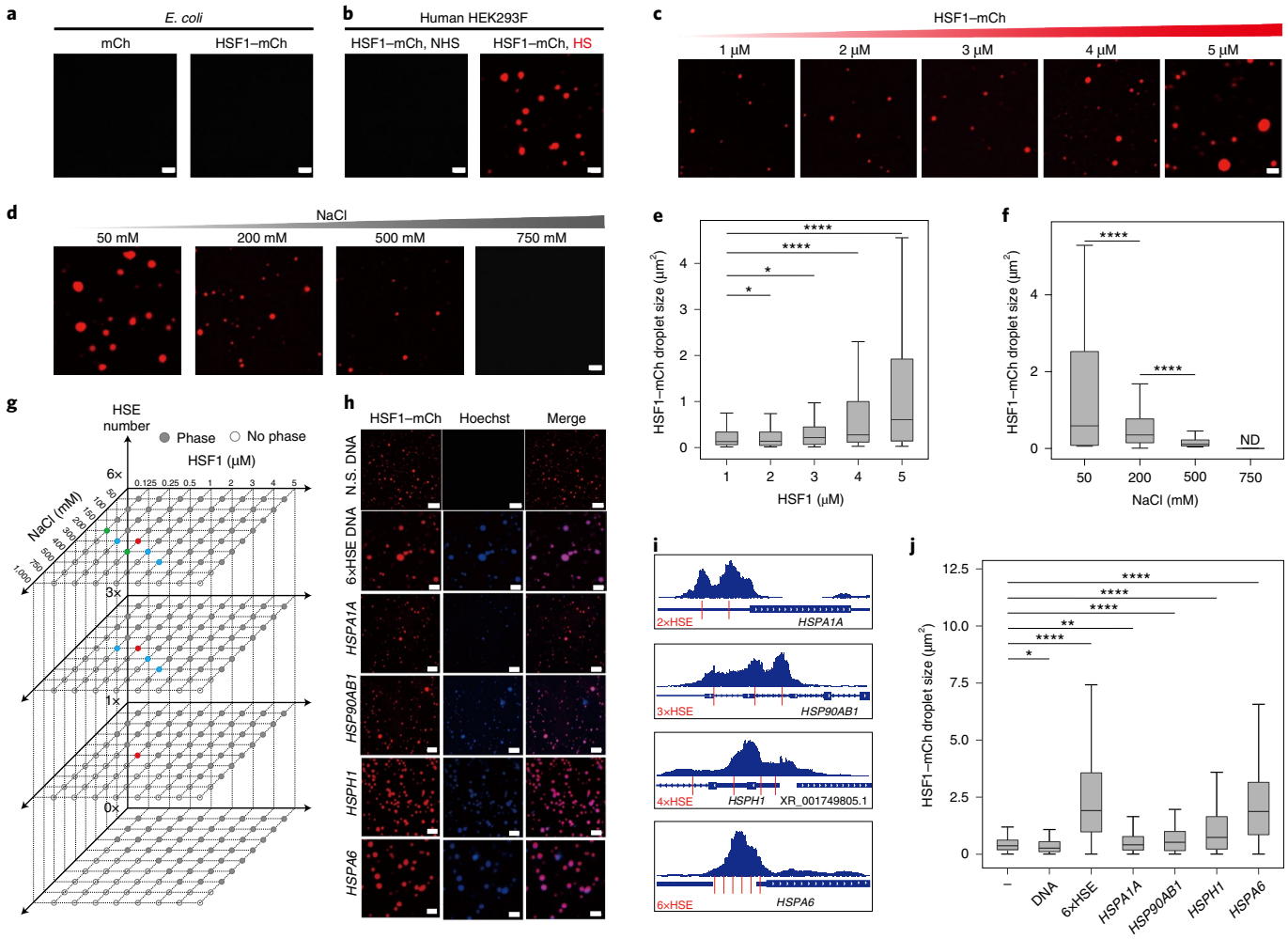

Fig. 2 | HSF1 undergoes LLPS in vitro. a,**b**, Representative images of droplet-formation assays performed with mCherry (mCh) and HSF1–mCh purified from *E. coli* (**a**), and HSF1–mCh purified from human HEK293F cells under NHS and HS (42 °C, 1 h) conditions (**b**). **c**,**d**, Fluorescence images of HSF1–mCh droplet formation in vitro in HEK293F cells under HS with the indicated concentrations of HSF1 (**c**) or 4 μM HSF1–mCh and the indicated NaCl concentrations (**d**). **a**–**d**, Scale bars, 2 μm. **e**, Sizes of HSF1–mCh droplets under different concentrations of HSF1–mCh; $n = 357$ (1 μM), 391 (2 μM), 158 (3 μM), 389 (4 μM) and 397 (5 μM) droplets in five fields pooled from five independent experiments. **f**, Sizes of HSF1–mCh droplets under different concentrations of NaCl; $n = 243$ (50 mM), 464 (200 mM), 1,135 (500 mM) and 0 (750 mM) droplets in five fields pooled from five independent experiments. ND, not determined. **g**, In vitro HSF1–mCh phase diagram under different HSF1–mCh and NaCl concentrations as well as HSE valencies. The coloured dots indicate emerging condensates compared with the lower layer. **h**, Fluorescence images showing HSF1–mCh (4 μM) co-phase separation with non-specific DNA, 6×HSE and DNA from the HSP genes. Scale bars, 3 μm. N.S., non-specific. **i**, Cut&Tag signals and HSE numbers for the promoters of HSP genes. The HSEs are indicated by red vertical lines. **j**, Sizes of HSF1–mCh droplets under different conditions; $n = 355$ (no DNA), 216 (non-specific DNA), 83 (6×HSE), 407 (*HSPA1A*), 524 (*HSP90AB1*), 361 (*HSPH1*) and 255 (*HSPA6*) droplets in five fields pooled from five independent experiments. **a**–**d**,**h**, Images are representative of five independent experiments. **e**,**f**,**j**, *P* values were determined using a paired two-tailed Student's *t*-test. Significant differences are labelled; $^{*}P < 0.05$, $^{**}P < 0.01$, $^{****}P < 0.0001$. **e**,**f**,**j**, In box plots, boxes show the 25th to the 75th percentile with the median, and whiskers indicate 1.5× the interquartile range.

We then studied the effects of DNA binding on HSF1 LLPS. When non-specific DNA was added to HSF1, the droplet sizes were similar to that of HSF1 alone. Larger droplets were formed with the addition of HSE (Fig. 2h). As heterogeneous copies of HSE exist in different HSF1 target genes (Extended Data Fig. 3e,f), we performed an in vitro reconstitution assay at various HSF1 concentrations and HSE valencies, and replotted the phase diagram (Fig. 2g). We found that the phase boundary of HSF1 could be shifted by a change in the number of copies of HSE, indicating an enhancement of LLPS. Furthermore, we found that, in addition to artificial HSE, endogenous HSEs, which are located upstream of HSP genes, could enhance HSF1 LLPS (Fig. 2h–j). These observations suggest that specific binding to multivalent DNA crowds HSF1 and thus lowers the threshold for LLPS, analogous to how enhancer DNA crowds transcription activators (BRD4 and MED1)[21] or methylated DNA enhances repressor (MeCP2)[30] LLPS. This phenomenon is also in line with the observation that HSF1 condensates tend to form at target gene loci (Fig. 1h). Together, these in vitro results demonstrate that HSF1 undergoes LLPS in response to HS and binding to DNA enhances its LLPS capability.

Inducible LLPS of HSF1 through PTMs. To identify which protein domains of HSF1 are responsible for LLPS, we generated five deletion mutants of HSF1 with deletions of the DNA-binding (DBD), LZ1–3, RD, LZ4 and activation (AD) domains—HSF1ΔDBD, HSF1ΔLZ1–3, HSF1ΔRD, HSF1ΔLZ4 and HSF1ΔAD, respectively—and explored their distribution in HS-treated cells. In comparison with full-length HSF1 and other deletion mutants, HSF1ΔRD

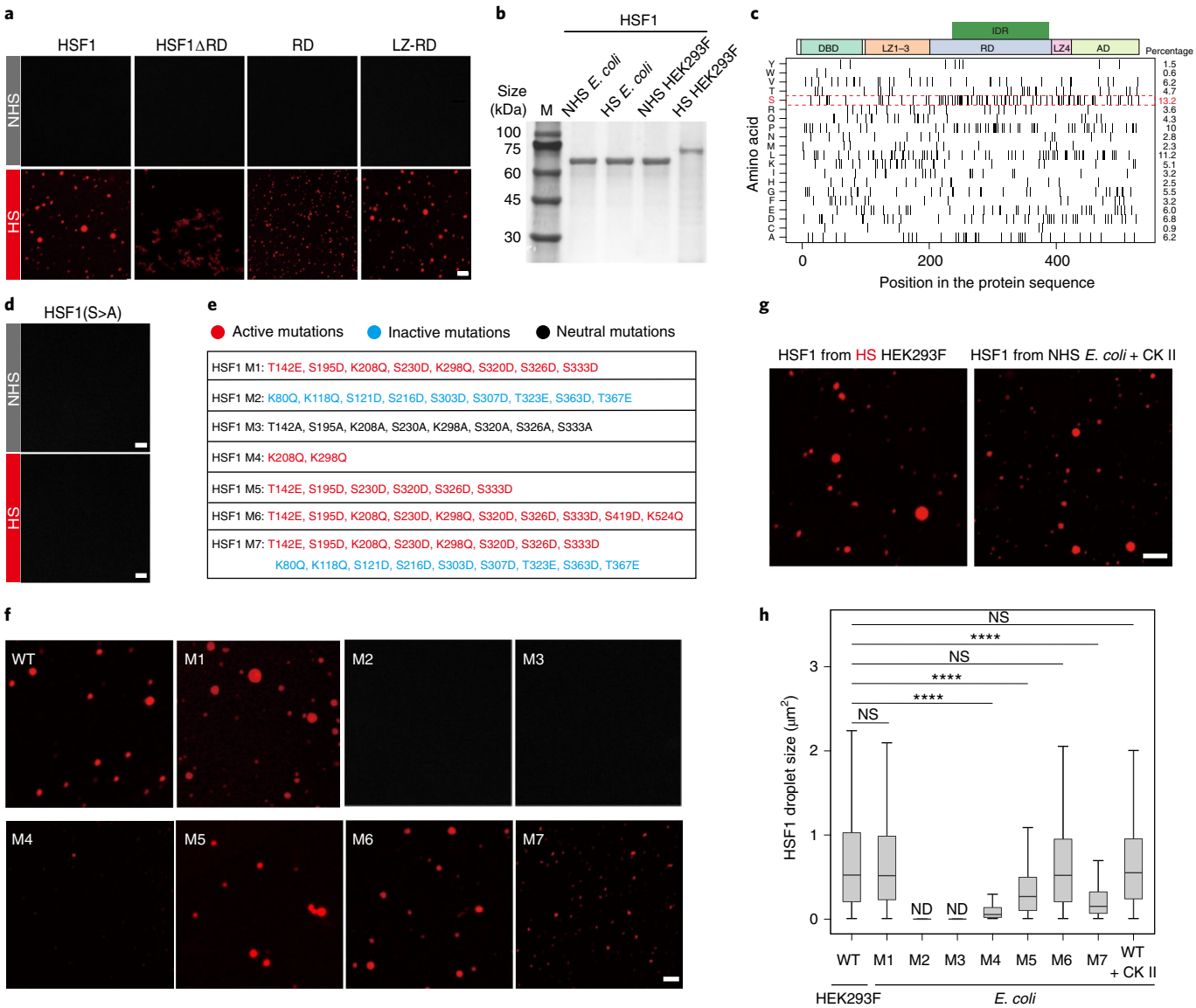

Fig. 3 | Post-translational modifications regulate LLPS of HSF1. a, Fluorescence images of droplet-formation assays of WT HSF1 and the HSF1ΔRD, RD and LZ-RD fragments purified from HEK293F cells in the absence (top) and presence of HS (42 °C, 1 h; bottom). Scale bars, 2 μm. **b**, Representative SDS–PAGE image showing HSF1–mCh protein purified from *E. coli* and HEK293F cells with and without HS treatment (42 °C, 1 h). **c**, Amino acid composition of the HSF1 protein. Each vertical line represents a single amino acid. The domain organization of HSF1 is shown (top). The red band indicates the content of serine in HSF1. **d**, Fluorescence images of droplet-formation assays of the S>A HSF1 mutant purified from HEK293F cells with and without HS treatment (42 °C, 1 h). Scale bars, 3 μm. **e**, Phosphorylation and acetylation sites in the HSF1 mutants M1–M7. S>D and T>E mutations were used to mimic constitutive phosphorylation, whereas the K>Q mutation was used to mimic constitutive acetylation. The S>A mutation mimics unphosphorylated HSF1. M1–M7 represent seven separate proteins with all of the indicated residues mutated simultaneously. **f**, Representative images of droplet-formation assays with the different HSF1 mutants. Scale bar, 2 μm. **g**, Representative images of droplet-formation assays with HSF1 from HS-treated (42 °C, 1 h) HEK293F cells and NHS *E. coli* phosphorylated by CK II. Scale bar, 3 μm. **h**, Droplet sizes in the cells from the different treatment groups in **f** and **g**; $n = 742$ (HSF1 WT), 723 (M1), 0 (M2 and M3), 243 (M4), 1,340 (M5), 770 (M6), 141 (M7) and 594 (HSF1 + CK II) droplets in five fields pooled from five independent experiments. *P* values were determined using a paired two-tailed Student's *t*-test. Significant differences are labelled; $^{****}P < 0.0001$. In box plots, boxes show the 25th to the 75th percentile with the median, and whiskers indicate 1.5× the interquartile range. **a**,**b**,**d**,**f**,**g**, Images are representative of five (**a**,**d**,**f**,**g**) or three (**b**) independent experiments.

and HSF1ΔLZ1–3 demonstrated substantially suppressed LLPS (Extended Data Fig. 4a–c). Owing to the deletion of the nuclear localization sequence, HSF1ΔRD in the cytoplasm was located to stress granules during HS, similar to other heat-denatured proteins (Extended Data Fig. 4d–f). Consistent with the in vivo observations, although full-length HSF1 purified from HS-treated HEK293F cells exhibited obvious LLPS in vitro (Fig. 2b–g), purified HSF1ΔRD from HS-treated HEK293F cells abolished LLPS capability (Fig. 3a), indicating the importance of the RD domain for HSF1 LLPS. However, the LLPS capability of the RD alone was impaired in comparison with full-length HSF1 (Fig. 3a). A truncation containing both the LZ1–3 and RD (LZ-RD) demonstrated similar LLPS to full-length HSF1 (Fig. 3a), suggesting that trimerization further increases the interaction valency of the RD. Together, these results showed that both the LZ1–3 and RD regions are required for HSF1 LLPS.

Many PTMs in the LZ1–3 and RD regions of HSF1 have been reported[11,31]. HSF1 purified from HS-treated HEK293F cells had a higher molecular weight than HSF1 from untreated cells (Fig. 3b). As the LZ1–3 and RD regions were responsible for HSF1 LLPS (Fig. 3a and Extended Data Fig. 4), PTMs in these domains following HS might explain why HSF1 from HS-treated HEK293F cells can undergo LLPS. The intrinsic disordered RD region of HSF1 is enriched for serine (Fig. 3c). To investigate whether HSF1 LLPS depends on this serine enrichment, we mutated all serine residues in the RD to alanine. The S>A HSF1 mutant (all serine residues mutated to alanine) failed to form droplets under both NHS and HS conditions in vitro (Fig. 3d), suggesting that HSF1 phase separation requires serine in its RD region.

Furthermore, the PTMs identified in the LZ1–3 and RD regions have been characterized as positive or negative PTMs according to their effects on the expression of HSF1 target genes through alanine scanning[6,31]. We wondered whether the opposite regulatory effects of different PTMs are the results of their effects on LLPS of HSF1. Therefore, we constructed simulative positive and negative mutants[32]—M1 and M2, respectively—and purified them from *E. coli* to evaluate their capacity for LLPS in vitro (Fig. 3e). Strikingly, consistent with their ability to activate transcription, M1 was found to phase separate to a similar extent to wild-type (WT) HSF1 purified from HS-treated HEK293F cells, whereas M2 remained dispersed in the solution, similar to WT HSF1 purified from untreated HEK293F cells or *E. coli* (Fig. 3f). We also created a neutral mutant, M3, to determine whether the absence of PTMs altered the LLPS behaviour of HSF1. M3 was unable to phase separate (Fig. 3f,g), suggesting that positive PTMs are required for HSF1 LLPS.

To explore whether both phosphorylation and acetylation contribute to HSF1 phase separation[33], we created two additional mutants, M4 and M5, to separate the effects of phosphorylation and acetylation on LLPS. In comparison with phosphorylation, acetylation had a minimal influence on HSF1 LLPS, as the majority of M4 remained dispersed, whereas M5 showed lower LLPS than M1 (Fig. 3f,h). We performed additional experiments to determine whether positive PTMs in the AD, in addition to the LZ1–3 and RD regions, contribute to LLPS by generating the M6 mutant; PTMs in the AD do not contribute significantly to HSF1 LLPS (Fig. 3f,h). Last, we created a mutant (M7) to explore the effects of simultaneous positive and negative PTMs in HSF1. The LLPS of M7 was compromised in comparison to M1 (Fig. 3f,h), further supporting that negative PTMs disfavour HSF1 LLPS.

In addition to mimicking PTM mutants, we induced phosphorylation of HSF1 using purified casein kinase II (CK II)[34,35] to directly test whether HSF1 phosphorylation modulates its LLPS. The CK II-phosphorylated HSF1 formed droplets comparable to HSF1 purified from HS-treated HEK293F cells or the positive PTM mimic M1 (Fig. 3g,h). Although numerous kinases might work in concert to control the phosphorylation of HSF1 during HS, we used CK II alone as proof of concept that phosphorylation of HSF1 plays a crucial role in controlling the LLPS of HSF1, thus modulating the HS transcriptional process.

HSF1 compartmentalizes transcription apparatuses. We examined whether the LLPS of HSF1 contributes to the rapid transcription during HS. We first showed that both HSF1 purified from HS-treated HEK293F cells and the positive PTM mimic M1 co-phase separated with RNA polymerase II (RNA pol II) carboxy (C)-terminal domain (CTD) repeat YSPTSPS, the super-enhancer markers BRD4 and MED1, and the transcriptional elongation machinery CYCT1 in vitro (Fig. 4a). The increased partition ratio of HSF1 in the co-phase separation system indicates that these transcription apparatuses could enhance the LLPS of HSF1 (Fig. 4b).

We next performed co-localization analyses to determine whether the formation of HSF1 condensates contributes to apparatus enrichment in cells. Using dual-colour STORM, we revealed that BRD4, RNA pol II with phosphorylated S5 or S2 (RNA pol II S5 and RNA pol II S2, respectively) and CYCT1 co-localized with HSF1 condensates in HS-treated HeLa cells but not the cells in the NHS group (Fig. 4c,e,f). In line with these results, we also detected the active transcription marker H3K4me3, but not the repressive marker H3K9me3, in the HSF1 condensates during HS (Fig. 4d,g,h). Together, these findings suggest that HSF1 condensates compartmentalize transcription apparatuses.

HSF1 LLPS promotes chromatin binding to HSP genes. To investigate whether the LLPS ability of HSF1 affects its chromatin association, we performed Cut&Tag, followed by high-throughput sequencing[36] to map the genome-wide distribution of LLPS-competent versus LLPS-incompetent HSF1 mutants under both NHS and HS conditions. We prepared *HSF1*-knockout cells and then infected these cells with lentivirus encoding HSF1 mutants (Extended Data Fig. 5a). Compared with WT HSF1 under NHS, both WT under HS and M1 under NHS showed increased and broad binding to enhancers and distal intergenic regions, with binding mostly enriched in the expected motifs of HSF-related transcription factors (Fig. 5a,b and Extended Data Fig. 5b–f). We next applied several strategies to determine the effect of LLPS on the chromatin occupancy of HSF1. First, we treated cells with 1,6-hexanediol and found it diminished the chromatin occupancy of both WT HSF1 under HS and the LLPS-competent mutant M1 under NHS conditions (Fig. 5a,b and Extended Data Fig. 5g,h). Second, we investigated the chromatin binding of the LLPS-deficient mutant M3, which showed decreased chromatin binding (Fig. 5a,b). This was not due to a loss of DNA-binding ability, as M3 was still capable of binding to HSE (Fig. 5c). The decreased chromatin occupancy instead reflects the loss of the intermolecular interaction that holds HSF1 LLPS. Furthermore, M3 in HS-treated cells showed similar reduced genomic targeting and shallow binding patterns to NHS

Fig. 4 | HSF1 compartmentalizes transcription apparatuses in LLPS condensates. a, Representative images of HSF1 and the HSF1 M1 mutant (4 μM each) co-phase separated with 10 μM RNA Pol II CTD, MED1, BRD4 and CYCT1. Scale bars, 3 μm. **b**, Partition ratios for the co-phase separations in **a**; $n = 1{,}933$ (HSF1), 3,698 (HSF1 + RNA Pol II CTD), 2,771 (HSF1 + MED1), 3,956 (HSF1 + BRD4), 1,396 (HSF1 + CYCT1), 895 (M1), 1,659 (M1 + RNA Pol II CTD), 534 (M1 + MED1), 1,530 (M1 + BRD4) and 2,128 (M1 + CYCT1) droplets in five fields pooled from five independent experiments. In box plots, boxes show the 25th to the 75th percentile with the median, and whiskers indicate 1.5× the interquartile range. **c**, Super-resolution images showing the co-localization of BRD4, RNA pol II S5, RNA pol II S2, and CYCT1 with HSF1 puncta with and without HS (42 °C, 0.5 h). Co-localization analysis was performed using the Imaris software (bottom). **d**, Co-localization of HSF1 condensates with repressive or active histone markers in HeLa cells under NHS and HS (42 °C, 0.5 h) conditions, viewed using immunofluorescence staining with anti-H3K9me3 or anti-H3K4me3. **c**,**d**, Scale bars, 2 μm (main images) and 100 nm (magnified views of the regions in the yellow boxes). **e**–**h**, Manders' coefficients showing the fraction of HSF1 overlapping different components of the transcription apparatuses (**e**), fraction of different components of the transcription apparatuses overlapping HSF1 (**f**), fraction of HSF1 overlapping epigenetic markers (**g**) and fraction of epigenetic markers overlapping HSF1 (**h**). Data are mean ± s.d.; $n = 11$ (H3K4m3 HS, H3K4m3 NHS, H3K9m3 NHS, RNA pol II S2 NHS and RNA pol II S5 NHS), 12 (H3K9m3 HS, CYCT1 HS, BRD4 HS, RNA pol II S2 HS, CYCT1 NHS and BRD4 NHS) and 8 (RNA pol II S5 HS) cells in five fields pooled from three independent experiments. **a**,**c**,**d**, Images are representative of five (**a**) or three (**c**,**d**) independent experiments. **b**,**e**–**h**, *P* values were determined using a paired two-tailed Student's *t*-test. Significant differences are labelled; $^{****}P < 0.0001$.

cells (Fig. 5a,b,d). Third, the enrichment of transcription apparatuses to HSF1 target genes also depended on whether HSF1 could phase separate at these sites (Fig. 5e,f and Extended Data Fig. 6). Finally, we conducted live-cell single-molecule imaging to evaluate the chromatin-binding kinetics of the LLPS-deficient mutant M3 relative to WT HSF1. Measurements of single-molecule

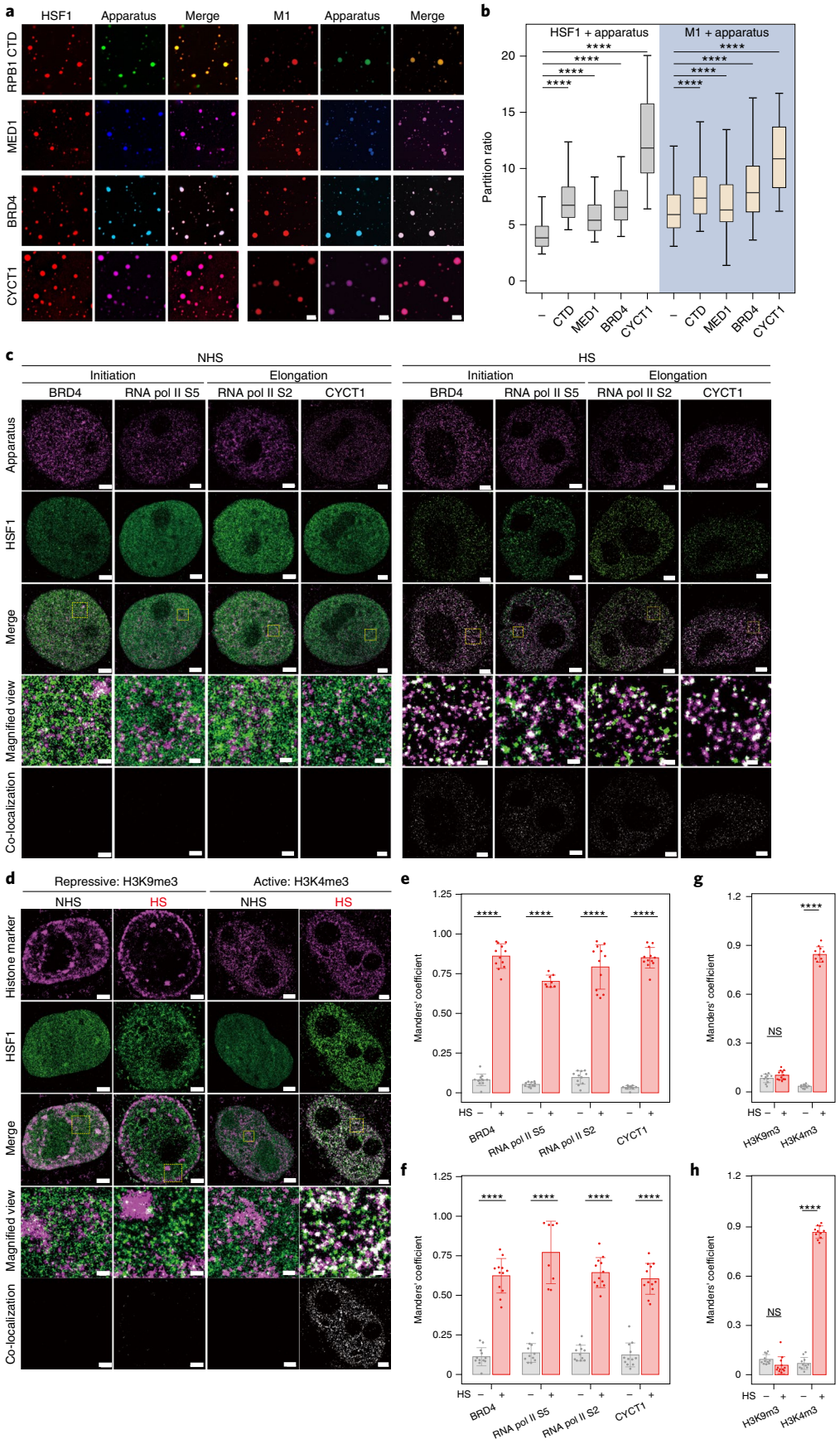

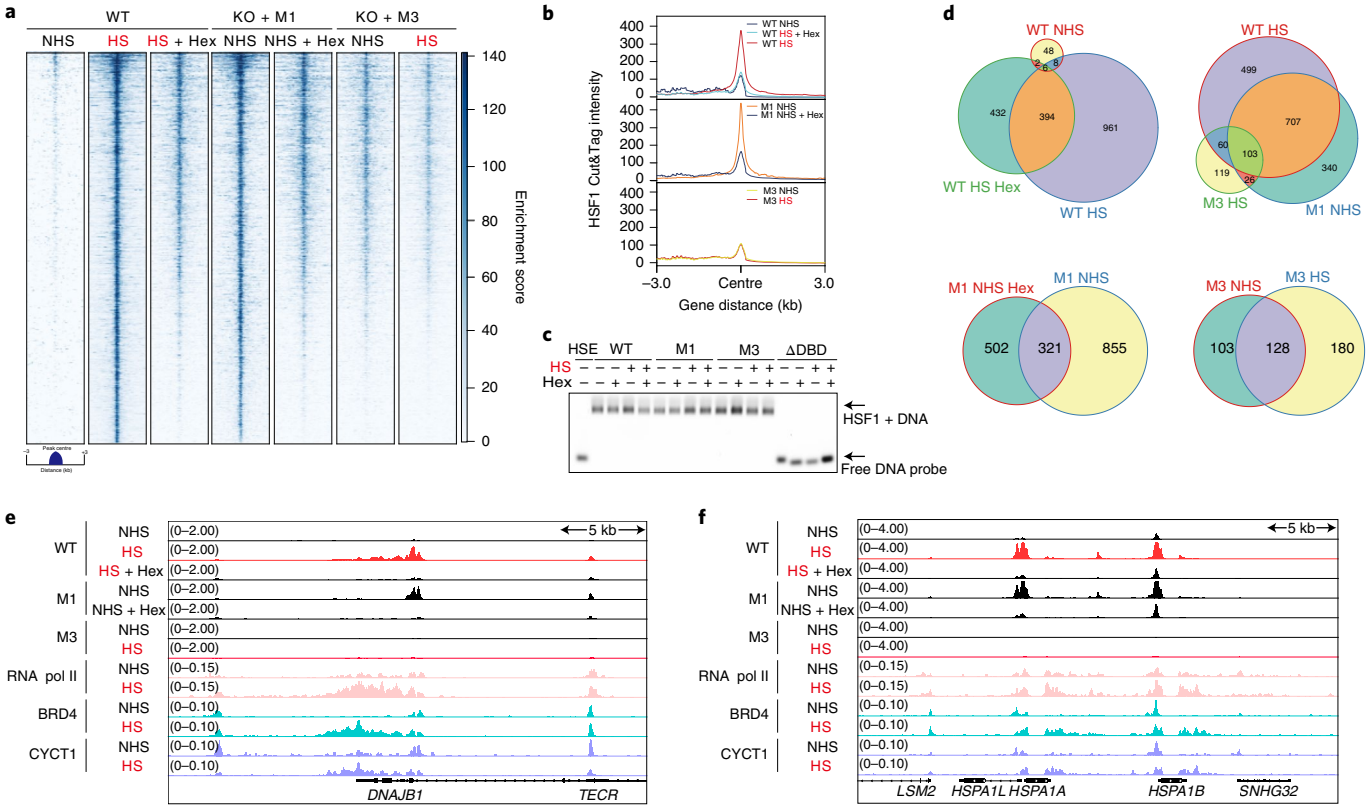

Fig. 5 | Phase separation markedly enhances the chromatin binding of HSF1. a, Heat maps for Cut&Tag signals in WT and *HSF1*-knockout (KO) HeLa cells transfected with the LLPS-competent M1 or LLPS-incompetent M3 HSF1 mutants under NHS and HS (42 °C, 0.5 h) conditions. The cells in the HS + 1,6-hexanediol (Hex) group were treated with 1.5% Hex for 30 min during HS. Images are representative of two independent experiments. **b**, Occupancy profile of HSF1 in Cut&Tag peaks averaged over all genomic regions under different conditions; 2,343 peak positions identified in WT cells under HS were used for comparison in all groups. **c**, EMSA showing the DNA-binding capability of WT HSF1, and the M1 and M3 mutants in the presence or absence of 10% Hex. HSF1ΔDBD was used as a negative control. Images are representative of three independent experiments. **d**, Venn diagrams showing the intersection of HSF1 Cut&Tag peaks under different conditions. **e**,**f**, Integrative Genome Viewer tracks of the indicated Cut&Tag signals (HSF1, RNA pol II, BRD4 and CYCT1) at the *DNAJB1* (**e**), and *HSPA1L*, *HSPA1A* and *HSPA1B* loci (**f**). Data are representative of two independent experiments.

displacement and diffusion coefficients showed that M3 was more mobile than WT HSF1 under HS conditions (Extended Data Fig. 2h–j and Supplementary Video 2), which suggests that M3 was not confined within phase-separated puncta. Super-resolution imaging of M3 also showed decreased cluster formation at HSP gene loci but maintained nSB formation (Extended Data Fig. 7). Together, the LLPS capability of HSF1 is essential for the efficient recruitment of HSF1 and transcription apparatuses to HSP gene loci.

HSF1 LLPS promotes the transcription of HSP genes. We next examined whether HSF1 LLPS in HS cells promotes the transcription of HSF1 target genes. We first globally labelled nascent RNA and explored their distribution with HSF1 condensates using STORM. Co-localization analyses indicated that most HSF1 condensates produce RNA during HS, suggesting that HSF1 condensates are active transcription hubs (Fig. 6a,b). We further performed HSP70 (*HSPA1L*) nascent RNA FISH and verified that the transcription foci of HSP70 are also located in the HSF1 condensates (Fig. 6c,d).

Next, we investigated whether interference with HSF1 LLPS affects the expression of its target genes using RNA sequencing (RNA-seq; Extended Data Fig. 8). We identified 249 differentially expressed genes that were significantly upregulated in HS-treated WT cells compared with untreated WT cells (Fig. 6e,f). LLPS-dependent gene activation was also observed in M1 cells under NHS conditions (Fig. 6e,f), in agreement with its increased chromatin-binding capability (Fig. 5a). In addition, the LLPS-incompetent M3 mutant showed lower HSP gene expression even under HS (Fig. 6e,f), which was also confirmed by quantitative PCR with reverse transcription (RT–qPCR) of HSP40 (*DNAJB1*) and HSP70 (*HSPA1A*; Fig. 6g,h). Thus, these data collectively support a crucial role for LLPS of HSF1 in activating the expression of HSP genes.

To further explore HSF1 LLPS as a general mechanism to promote the expression of target genes, we constructed a transcriptional-activation reporter assay by fusing the Gal4 DBD with different HSF1 mutants and truncations in a reporter cell line to decouple the binding of HSF1 to DNA and LLPS (Fig. 6i). Both the LZ1–3 and RD regions, which are responsible for HSF1 LLPS, further increased reporter expression in comparison with AD only (Fig. 6j). Cells transfected with the M1 mutant showed the highest level of reporter expression. Furthermore, when the HSF1 AD was replaced with VP16, an AD derived from the herpes simplex virus[37], both RD and RD (M1 active) also enhanced its transcriptional activity (Fig. 6k). Last, we substituted the RD region with the IDR (amino acids 1–218) of FUS (FUS-N), which is well known for its strong LLPS ability[38]. This chimaeric protein was able to enhance transcription of the reporter gene to a level similar to that induced by RD (M1 active) (Fig. 6l). Together, these results suggest that LLPS of HSF1 is the key mechanism underlying the fast and vast transcriptional response under HS.

Furthermore, we explored whether LLPS of HSF1 regulates gene expression under non-acute stress conditions. HSF1 plays a role in

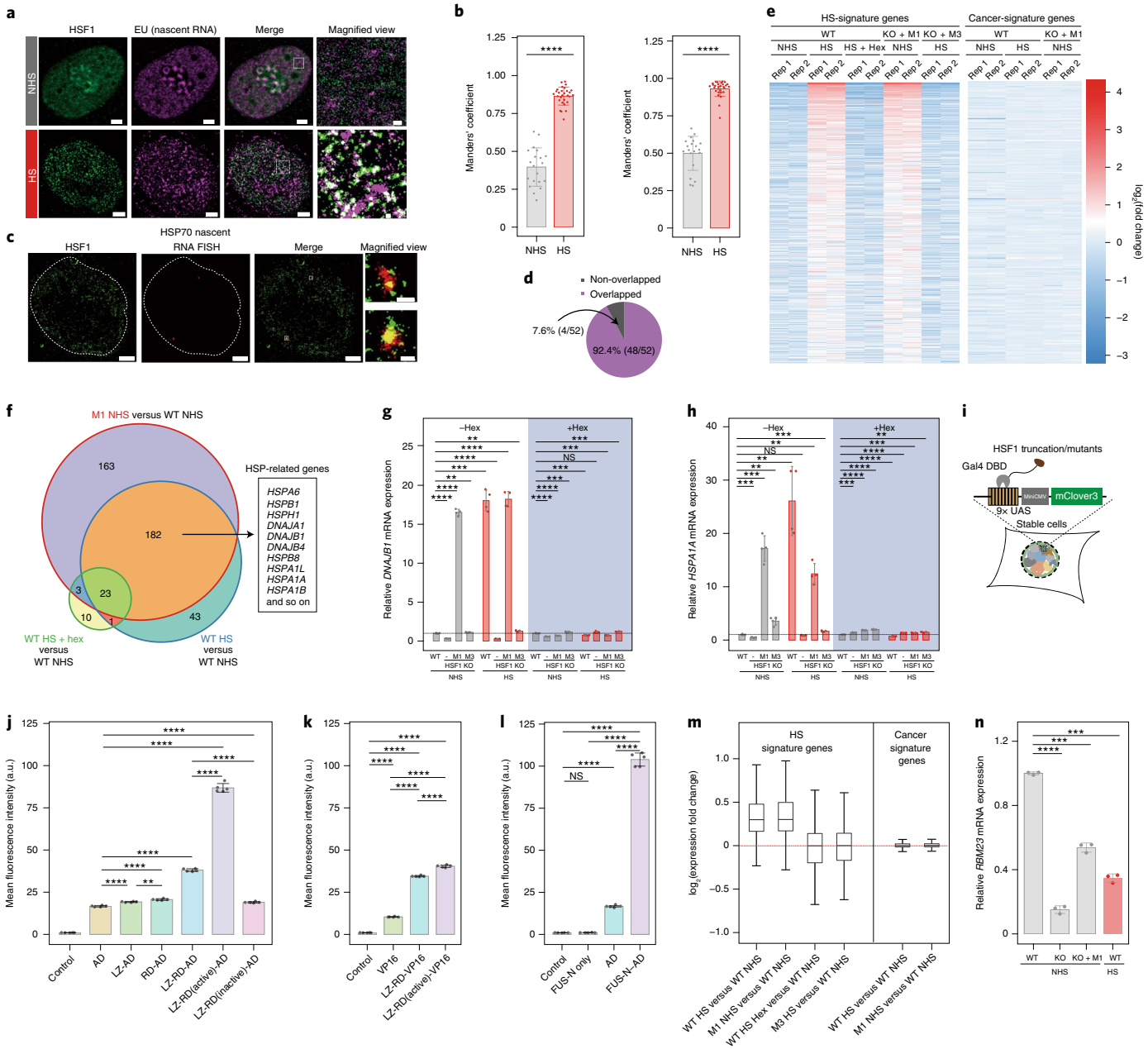

Fig. 6 | Phase separation of HSF1 promotes HSP-gene transcription. a, Super-resolution images showing the co-localization of HSF1 condensates with nascent RNA under NHS and HS (42 °C, 0.5 h) conditions. Scale bars, 2 µm (main images) and 100 nm (magnified views of the regions in the white boxes). EU, 5-ethynyl uridine **b**, Manders' coefficients showing the fraction of 5-ethynyl uridine overlapping with HSF1 condensates (left) and HSF1 condensates overlapping with 5-ethynyl uridine (right) under NHS and HS (42 °C, 0.5 h) conditions; $n = 20$ (NHS) and 29 (HS) cells pooled from three independent experiments. **c**, Super-resolution images showing the co-localization of HSF1 condensates with HSP70 (*HSPA1L*) nascent RNA under HS (42 °C, 0.5 h). The dotted white line represent the outline of the nucleus. Scale bars, 2 µm (main images) and 200 nm (magnified views of the regions in the white boxes). **d**, Percentage of HSF1 condensates that overlap with HSP70 nascent RNA. **e**, Heat map of HS- and cancer-signature genes under different conditions. HS + Hex, treatment with 1.5% 1,6-hexanediol for 1 h during HS at 42 °C; Rep, replicate. **f**, Relationship between different groups of differentially expressed genes, with a battery of HSP genes highlighted. **g**,**h**, Levels of *DNAJB1* (**g**) and *HSPA1A* (**h**) messenger RNA, determined by RT–qPCR, in WT and *HSF1*-knockout cells transfected with various HSF1 mutants; $n = 4$ biologically independent samples. **i**, Schematic of the transcriptional-activation reporter assay. UAS, upstream activation sequence. **j**–**l**, Fluorescence intensity of mClover3 in reporter cells under different conditions: different truncations of HSF1 (**j**); fusion protein of IDR of HSF1 with VP16 (**k**); fusion protein of the activation domain of HSF1 with phase separation protein FUS_N (**l**); $n = 5$ biologically independent samples; a.u., arbitrary units. **m**, Changes in expression for all HS-signature and cancer-signature target genes of HSF1. All of the groups were compared with WT cells under NHS conditions; $n = 677$ (HS) and 429 (cancer) genes were analysed. In box plots, boxes show the 25th to the 75th percentile with the median, and whiskers indicate 1.5× the interquartile range. **n**, Levels of *RBM23* mRNA, determined by RT–qPCR, in WT and *HSF1*-knockout cells transfected with M1; $n = 3$ biologically independent samples. **a**,**c**, Images are representative of three independent experiments. **b**,**g**,**h**,**j**–**l**,**n**, Data are mean ± s.d. *P* values were determined using a paired two-tailed Student's *t*-test. Significant differences are labelled; $^{**}P < 0.01$, $^{***}P < 0.001$, $^{****}P < 0.0001$. KO, *HSF1* knockout.

tumorigenesis by changing either expression or PTMs, including phosphorylation of serine 326 (S326P)[39,40]. Therefore, we explored whether HSF1 S326P can initiate LLPS by assessing the LLPS of HSF1 (S326D) both in vivo and in vitro. The failure of HSF1 (S326D) to undergo LLPS indicated that transcriptional activation of HSF1 in malignant cells is not due to increased LLPS capability (Extended Data Fig. 9a). We then revisited our RNA-seq results and found that cancer-specific HSF1 target genes were not activated in HS-treated WT cells and NHS M1 cells (Fig. 6e,m), which further demonstrated that genes activated by HSF1 in cancers were not controlled by LLPS of HSF1. This result is consistent with the previous finding that the occupancy of HSF1 at cancer-specific genes decreases during HS[5]. We also confirmed this result by RT–qPCR of one of these genes, *RBM23* (ref. [5]), which was repressed under HS conditions and did not respond to M1 (Fig. 6n), indicating that LLPS of HSF1 did not control the expression of the cancer-specific genes. We also verified these results in various cancer cell lines. The failure to activate *RBM23* expression and the success to activate *HSPA1A* expression in these cancer cell lines under HS or M1-overexpression conditions (Extended Data Fig. 9b–j) further indicated the conservation of the mechanism that HSF1 activates target expression via different mechanisms under HS and in cancers.

HSP70 disrupts HSF1 LLPS and alleviates phase transition. As extended HS causes cell death, we next investigated whether prolonged HS influences HSF1 phase transition. We incubated HeLa cells at 42 °C for various time periods and performed fluorescence recovery after photobleaching (FRAP) to evaluate the liquidity of HSF1 condensates. The recovery of HSF1 droplets in cells exposed to HS for 4 h was much lower than for cells exposed to HS for 1 h (Fig. 7a,b), suggesting a liquid-to-gel phase transition of HSF1 following extended HS. In line with the experiments in living cells, gelation of purified HSF1 condensates in vitro was also observed following prolonged incubations (Fig. 7c,d). Intriguingly, the presence of a low concentration of HSP70 was able to maintain the round morphology of HSF1 condensates and prevent them from undergoing aggregation and gelation even after 24 h of incubation (Fig. 7c,d), suggesting that HSP70 may disrupt the phase transition of HSF1. Next, we overexpressed HSP70 in living cells to investigate the inhibitory effect of HSP70 on HSF1 LLPS. We observed that HSF1 nSBs became less abundant and small condensates were more dispersed in cells with HSP70 overexpression (Fig. 7e–h).

Next, we investigated how HSP70 interferes with LLPS of HSF1. The LLPS tendency of HSP70 alone was weak (Extended Data Fig. 10a) but HSP70 was observed in HSF1 droplets at low HSP70 concentrations (Fig. 7i), in line with the interaction between HSP70 and HSF1 (ref. [41]). When HSF1 was incubated with a high concentration of HSP70 in the co-phase separation system, HSF1 no longer formed droplets (Fig. 7i,j). Consistent with these data, when a high concentration of HSP70 was added to pre-formed HSF1 droplets, the HSF1 droplets dissolved rapidly (Extended Data Fig. 10b). As ATP hydrolysis regulates the chaperone cycle of HSP70, binding of substrates to HSP70·ATP triggers ATP hydrolysis and transition to the ADP-bound state, which has a high affinity for the substrate[42]. When ATP was added to the LLPS buffer, HSP70 could not dissolve HSF1 droplets (Extended Data Fig. 10c,d). This might reveal that the interaction strength of ATP-bound HSP70 and HSF1 is lower than the intermolecular interaction between HSF1 molecules, making the dissolution process unfavourable. To identify the domains of HSP70 that contribute to the disruption of HSF1 phase separation, we split HSP70 into an amino (N)-terminal nucleotide-binding domain (NBD; amino acids 1–385) and a C-terminal substrate-binding domain (SBD; amino acids 386–641)[42]. We found that the SBD, rather than the NBD, conferred HSP70 with the ability to dissolve HSF1 condensates (Fig. 7e,k). Furthermore, the SBD also inhibited RD LLPS, indicating that HSP70 binds to the RD region to disrupt LLPS of HSF1 (Fig. 7k).

We next explored whether this phenomenon is HSP70-specific. Among a broad spectrum of HSP40 proteins, we chose three proteins (*DNAJA1*, *DNAJA2* and *DNAJB1*) from different HSP40 classes as well as HSP90 (*HSPCA*) to test their ability to dissolve HSF1 droplets. Neither the HSP40 proteins nor HSP90 were able to dissolve HSF1 condensates (Extended Data Fig. 10e), suggesting that the negative regulation of HSF1 phase separation during HS is chaperon-specific.

Discussion

Here we presented evidence showing that HSF1 forms local high-concentration hubs via co-phase separation with the transcriptional machinery at endogenous HSP loci. Importantly, we demonstrated that small HSF1 condensates, rather than the canonical prominent nSBs, promote transcription during HS. Although previous work demonstrated that nSBs are formed by phase transition of HSF1 (ref. [9]), here we proved that HSF1 forms condensates at both nSBs and HSP-gene foci. The difference between these two distinct structures depends on the copy number of the HSF1 binding sites embedded in these sequences[25] (Fig. 1d). Given the observations that prominent nSBs are not co-localized with HSP genes[7] and correlated negatively with their expression[9], we speculate that HSF1 LLPS may play a multifold role in transcriptional regulation under acute stress. These distinct distributions of HSF1 in nSBs and HSP-gene puncta may indicate their different functions. Nuclear stress bodies and HSP gene puncta might coordinate to effectively cope with acute stress by shutting down unnecessary gene expression

Fig. 7 | HSP70 prevents HSF1 condensates from undergoing a gel-like phase transition under prolonged HS stress. a,**b**, FRAP images (**a**) as well as the fluorescence intensity (**b**, left) and relative recovery (**b**, right) of HSF1 droplets in cells exposed to HS at 42 °C for 1, 2 and 4 h. Scale bar, 1 μm; $n = 10$ (1 h), 12 (2 h) and 10 (4 h) cells from three independent experiments. **c**, Fluorescence images of HSF1–mCh (4 μM) droplets with HSP70 at different concentrations (0, 0.4, 0.8 and 8 μM from left to right) at room temperature (RT) for 0, 12 and 24 h. Scale bars, 2 μm. **d**, FRAP analysis of HSF1 (4 μM) with or without HSP70 (0.4 μM) at RT for 0, 12 and 24 h; $n = 16$ droplets from three independent experiments in each group. **e**,**f**, Images of nSBs in cells expressing full-length (FL) HSP70, the N-terminal NBD of HSP70 (HSP70-N) or the C-terminal SBD domain of HSP70 (HSP70-C; **e**), and the ratio of cells with nSBs (**f**). Scale bars, 10 μm; $n = 6$ (HSF1), 7 (HSF1–HSP70 and HSF1–HSP70-N) and 12 (HSF1–HSP70-C) views from three independent experiments. **g**,**h**, Super-resolution images (**g**) and the intensity heterogeneity index (**h**) of HSF1 condensates in control (WT) and HSP70-overexpressing (OE) cells under HS (42 °C, 0.5 h). Scale bars, 2 μm (main images) and 200 nm (magnified views of the regions in the white boxes); $n = 12$ cells from three independent experiments for each group. **i**,**j**, Fluorescence images of in vitro HSF1–mCh (4 μM) droplet formation under different HSP70 concentrations (0.4, 0.8, 2.0, 4.0, 6.0 and 8.0 μM from left to right; **i**) and the HSF1 droplet size in the respective groups (**j**). Scale bars, 2 μm; $n = 1{,}206$ (0 μM HSP70), 1,437 (0.4 μM), 637 (0.8 μM), 4,601 (2 μM), 2,397 (4 μM), 647 (6 μM) and 0 (8 μM) droplets in five fields from five independent experiments. ND, not determined. **j**, In box plots, boxes show the 25th to the 75th percentile with the median, and whiskers indicate 1.5× the interquartile range. **k**, Fluorescence images of in vitro HSF1–mCh (4 μM, left) and RD–mCh (4 μM, right) droplets with 8 μM HSP70-FL (top), HSP70-N (middle) and HSP70-C (bottom). Scale bars, 2 μm. **l**, Inducible and reversible LLPS of HSF1 mediates the transcriptional response during HS. **b**,**d**,**f**,**h**, Data are mean ± s.d. **a**,**c**,**e**,**g**,**i**,**k**, Images are representative of three (**a**,**e**,**g**) or five (**c**,**i**,**k**) independent experiments. **b**,**h**,**j**, *P* values were determined using a paired two-tailed Student's *t*-test. Significant differences are labelled; $^{****}P < 0.0001$, $^{***}P < 0.001$, $^{*}P < 0.05$.

while maintaining maximum transcription of HSPs. HSF1 in nSBs transcribes the highly repetitive satellite III long noncoding RNA, which mediates global gene repression through the sequestration of transcription apparatuses into nSBs and protects against HS-induced cell death[28,43–45]. Meanwhile, the effective concentration of HSF1 in the nucleoplasm decreased dramatically due to the trapping of HSF1 within nSBs. Multivalent weak interaction/cluster formation of HSF1 at HSP foci could effectively increase its local

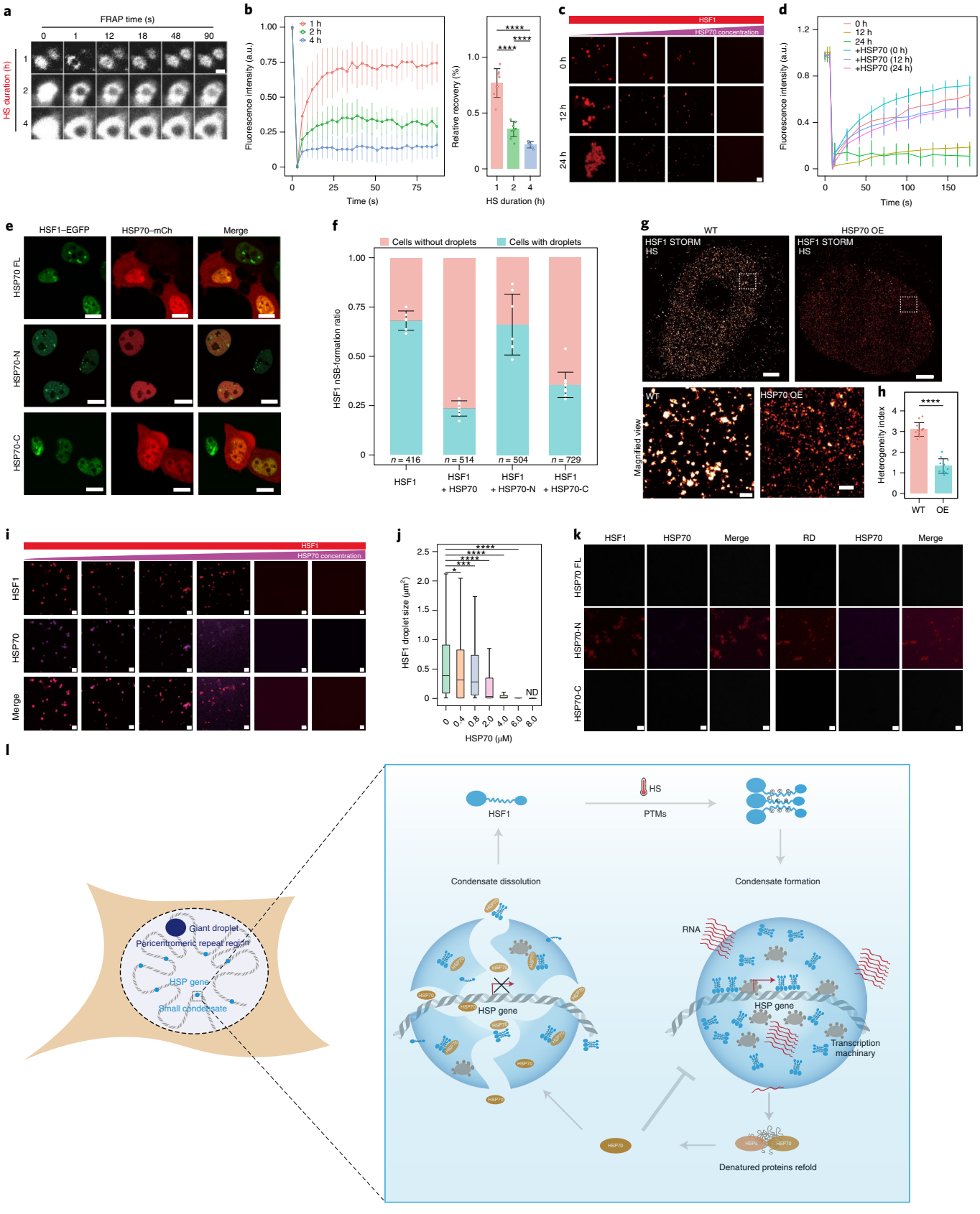

concentration to induce rapid transcription during HS. The allocation of HSF1 between these two statuses might be fine-tuned as an effective strategy to balance the rapid transient activation of HSP expression and global transcription during HS.

How nearby phosphorylation sites in the LZ1–3 and RD regions oppositely regulate HSF1 transcription activity has been a long-standing question, but our finding that different PTM patterns are linked to HSF1 LLPS provides a mechanism for this effect. Positive PTMs of LLPS increase transcription, whereas negative PTMs of LLPS decrease HSP-gene expression. In contrast to HS, HSF1 does not employ LLPS to activate transcription in cancers, indicating that LLPS of HSF1 is a necessary mechanism for cells to effectively cope with acute stress.

Attenuation of HS is a crucial process that allows cells to restore protein homeostasis following the cessation of HS. We discovered that HSP70 can disrupt HSF1 LLPS. A recent study showed that HSP70 regulates HSF1 activity by trimer unzipping and dissociation from DNA[46]. We may have identified the processes acting upstream of this mechanism. First, HSP70 undergoes co-phase separation with HSF1 and accumulates within HSF1 droplets, after which the resulting high concentration of HSP70 mediates droplet dissolution. After HSF1 condensate dissolution, HSP70 unzips the chromatin-binding trimeric HSF1, leading to HSF1 dissociation from DNA. Importantly, this mechanism is essential for preventing functional HSF1 liquid condensates from undergoing a gel-like, nocuous phase transition under prolonged HS stress. Several recent studies have shown that HSPs can prevent protein phase transitions, thus maintaining proteins in a liquid state[47–49]. This inducible and reversible phase-separation feedback mechanism provides crucial, previously unknown information about how dynamic regulation of HSF1 activity drives transcriptional responses and attenuates HS to maintain protein homeostasis during acute stress (Fig. 7l).

Online content

Any methods, additional references, Nature Research reporting summaries, source data, extended data, supplementary information, acknowledgements, peer review information; details of author contributions and competing interests; and statements of data and code availability are available at https://doi.org/10.1038/s41556-022-00846-7.

Received: 27 February 2021; Accepted: 10 January 2022;
Published online: 7 March 2022

References

1. Lindquist, S. The heat-shock response. *Annu. Rev. Biochem.* **55**, 1151–1191 (1986).
2. Mahat, D. B., Salamanca, H. H., Duarte, F. M., Danko, C. G. & Lis, J. T. Mammalian heat shock response and mechanisms underlying its genome-wide transcriptional regulation. *Mol. Cell* **62**, 63–78 (2016).
3. Richter, K., Haslbeck, M. & Buchner, J. The heat shock response: life on the verge of death. *Mol. Cell* **40**, 253–266 (2010).
4. Gomez-Pastor, R. et al. Abnormal degradation of the neuronal stress-protective transcription factor HSF1 in Huntington's disease. *Nat. Commun.* **8**, 14405 (2017).
5. Mendillo, M. L. et al. HSF1 drives a transcriptional program distinct from heat shock to support highly malignant human cancers. *Cell* **150**, 549–562 (2012).
6. Gomez-Pastor, R., Burchfiel, E. T. & Thiele, D. J. Regulation of heat shock transcription factors and their roles in physiology and disease. *Nat. Rev. Mol. Cell Biol.* **19**, 4–19 (2018).
7. Jolly, C., Morimoto, R., Robert-Nicoud, M. & Vourc'h, C. HSF1 transcription factor concentrates in nuclear foci during heat shock: relationship with transcription sites. *J. Cell Sci.* **110**, 2935–2941 (1997).
8. Chowdhary, S., Kainth, A. S., Pincus, D. & Gross, D. S. Heat shock factor 1 drives intergenic association of its target gene loci upon heat shock. *Cell Rep.* **26**, 18–28 (2019).
9. Gaglia, G. et al. HSF1 phase transition mediates stress adaptation and cell fate decisions. *Nat. Cell Biol.* **22**, 151–158 (2020).
10. Denegri, M. et al. Human chromosomes 9, 12, and 15 contain the nucleation sites of stress-induced nuclear bodies. *Mol. Biol. Cell* **13**, 2069–2079 (2002).
11. Xu, Y. M., Huang, D. Y., Chiu, J. F. & Lau, A. T. Post-translational modification of human heat shock factors and their functions: a recent update by proteomic approach. *J. Proteome Res.* **11**, 2625–2634 (2012).
12. Kline, M. P. & Morimoto, R. I. Repression of the heat shock factor 1 transcriptional activation domain is modulated by constitutive phosphorylation. *Mol. Cell Biol.* **17**, 2107–2115 (1997).
13. Kourtis, N. et al. FBXW7 modulates cellular stress response and metastatic potential through HSF1 post-translational modification. *Nat. Cell Biol.* **17**, 322–332 (2015).
14. Hietakangas, V. et al. Phosphorylation of serine 303 is a prerequisite for the stress-inducible SUMO modification of heat shock factor 1. *Mol. Cell. Biol.* **23**, 2953–2968 (2003).
15. Lu, Y. et al. Phase separation of TAZ compartmentalizes the transcription machinery to promote gene expression. *Nat. Cell Biol.* **22**, 453–464 (2020).
16. Cai, D. et al. Phase separation of YAP reorganizes genome topology for long-term YAP target gene expression. *Nat. Cell Biol.* **21**, 1578–1589 (2019).
17. Hnisz, D., Shrinivas, K., Young, R. A., Chakraborty, A. K. & Sharp, P. A. A phase separation model for transcriptional control. *Cell* **169**, 13–23 (2017).
18. Guo, Y. E. et al. Pol II phosphorylation regulates a switch between transcriptional and splicing condensates. *Nature* **572**, 543–548 (2019).
19. Lu, H. et al. Phase-separation mechanism for C-terminal hyperphosphorylation of RNA polymerase II. *Nature* **558**, 318–323 (2018).
20. Boehning, M. et al. RNA polymerase II clustering through carboxy-terminal domain phase separation. *Nat. Struct. Mol. Biol.* **25**, 833–840 (2018).
21. Cho, W. K. et al. Mediator and RNA polymerase II clusters associate in transcription-dependent condensates. *Science* **361**, 412–415 (2018).
22. Chong, S. et al. Imaging dynamic and selective low-complexity domain interactions that control gene transcription. *Science* **361**, eaar2555 (2018).
23. Sabari, B. R. et al. Coactivator condensation at super-enhancers links phase separation and gene control. *Science* **361**, eaar3958 (2018).
24. Obradovic, Z. et al. Predicting intrinsic disorder from amino acid sequence. *Proteins* **53**, 566–572 (2003).
25. Jolly, C. et al. In vivo binding of active heat shock transcription factor 1 to human chromosome 9 heterochromatin during stress. *J. Cell Biol.* **156**, 775–781 (2002).
26. Cotto, J., Fox, S. & Morimoto, R. HSF1 granules: a novel stress-induced nuclear compartment of human cells. *J. Cell Sci.* **110**, 2925–2934 (1997).
27. Shin, Y. et al. Spatiotemporal control of intracellular phase transitions using light-activated optodroplets. *Cell* **168**, 159–171 (2017).
28. Jolly, C. et al. Stress-induced transcription of satellite III repeats. *J. Cell Biol.* **164**, 25–33 (2004).
29. Rust, M. J., Bates, M. & Zhuang, X. Sub-diffraction-limit imaging by stochastic optical reconstruction microscopy (STORM). *Nat. Methods* **3**, 793–795 (2006).
30. Li, C. H. et al. MeCP2 links heterochromatin condensates and neurodevelopmental disease. *Nature* **586**, 440–444 (2020).
31. Guettouche, T., Boellmann, F., Lane, W. S. & Voellmy, R. Analysis of phosphorylation of human heat shock factor 1 in cells experiencing a stress. *BMC Biochem.* **6**, 4 (2005).
32. Chen, Z. & Cole, P. A. Synthetic approaches to protein phosphorylation. *Curr. Opin. Chem. Biol.* **28**, 115–122 (2015).
33. Raychaudhuri, S. et al. Interplay of acetyltransferase EP300 and the proteasome system in regulating heat shock transcription factor 1. *Cell* **156**, 975–985 (2014).
34. Zheng, X. et al. Dynamic control of Hsf1 during heat shock by a chaperone switch and phosphorylation. *eLife* **5**, e18638 (2016).
35. Gerber, D. A. et al. Heat-induced relocalization of protein kinase CK2. Implication of CK2 in the context of cellular stress. *J. Biol. Chem.* **275**, 23919–23926 (2000).
36. Kaya-Okur, H. S. et al. CUT&Tag for efficient epigenomic profiling of small samples and single cells. *Nat. Commun.* **10**, 1930 (2019).
37. Moriuchi, H. et al. Hydrophobic cluster analysis predicts an amino-terminal domain of varicella-zoster virus open reading frame 10 required for transcriptional activation. *Proc. Natl Acad. Sci. USA* **92**, 9333–9337 (1995).
38. Dine, E., Gil, A. A., Uribe, G., Brangwynne, C. P. & Toettcher, J. E. Protein phase separation provides long-term memory of transient spatial stimuli. *Cell Syst.* **6**, 655–663 (2018).
39. Dai, C. & Sampson, S. B. HSF1: guardian of proteostasis in cancer. *Trends Cell Biol.* **26**, 17–28 (2016).
40. Tang, Z. et al. MEK guards proteome stability and inhibits tumor-suppressive amyloidogenesis via HSF1. *Cell* **160**, 729–744 (2015).
41. Shi, Y., Mosser, D. D. & Morimoto, R. I. Molecular chaperones as HSF1-specific transcriptional repressors. *Genes Dev.* **12**, 654–666 (1998).
42. Rosenzweig, R., Nillegoda, N. B., Mayer, M. P. & Bukau, B. The Hsp70 chaperone network. *Nat. Rev. Mol. Cell Biol.* **20**, 665–680 (2019).
43. Weighardt, F. et al. A novel hnRNP protein (HAP/SAF-B) enters a subset of hnRNP complexes and relocates in nuclear granules in response to heat shock. *J. Cell Sci.* **112**, 1465–1476 (1999).

44. Goenka, A. et al. Human satellite-III non-coding RNAs modulate heat-shock-induced transcriptional repression. *J. Cell Sci.* **129**, 3541–3552 (2016).
45. Ninomiya, K. et al. LncRNA-dependent nuclear stress bodies promote intron retention through SR protein phosphorylation. *EMBO J.* **39**, e102729 (2020).
46. Kmiecik, S. W., Le Breton, L. & Mayer, M. P. Feedback regulation of heat shock factor 1 (Hsf1) activity by Hsp70-mediated trimer unzipping and dissociation from DNA. *EMBO J.* **39**, e104096 (2020).
47. Liu, Z. et al. Hsp27 chaperones FUS phase separation under the modulation of stress-induced phosphorylation. *Nat. Struct. Mol. Biol.* **27**, 363–372 (2020).
48. Yu, H. et al. HSP70 chaperones RNA-free TDP-43 into anisotropic intranuclear liquid spherical shells. *Science* **371**, eabb4309 (2021).
49. Gu, J. et al. Hsp40 proteins phase separate to chaperone the assembly and maintenance of membraneless organelles. *Proc. Natl Acad. Sci. USA* **117**, 31123–31133 (2020).

Methods

Plasmid construction, cell culture and transfection. We amplified all complementary DNA sequences from a cDNA library produced from HeLa S6 cells by reverse transcription. All constructs were generated using Gibson assembly. Site-direct mutagenesis (Thermo Fisher Scientific, A14603) was used to create all plasmids for all of the HSF1 mutants (M1–M7). The S>A HSF1 mutant was directly synthesised by Ruibo Biotech (Beijing). Other truncations of HSF1 were generated through PCR amplification of full-length HSF1 and then cloned into a vector through Gibson assembly. Detailed information on the plasmids can be found in Supplementary Table 1.

The human cancer cell line HeLa S6 was cultured in DMEM medium (Gibco) containing 10% fetal bovine serum (Lifetech), and 50 μg ml^{-1} penicillin and streptomycin (Lifetech). The cells were maintained in a humidified incubator at 37 °C with an atmosphere containing 5% CO_2. One day before transfection, the cells were passaged into a 35 mm Petri dish at a density of approximately 50%. Transfection of cells was performed using Lipofectamine 3000 (Lifetech) following the manufacturer's protocol. The plasmids (approximately 1 μg) were transfected into cells in a six-well plate or 35 mm Petri dish for all conditions, unless otherwise indicated. For HS, the cells were heated for 30 min or 1 h in an incubator pre-warmed to 42 °C, as indicated in the figure legends.

For RNA interference of HSF1, small interfering RNAs (siRNAs; sense: 5′-CCAAGUACUUCAAGCACAATT-3′, 5′-CCAGUAUCCAAGAGCUCCUTT-3′ and 5′-GCAUGCCCAGCAACAGAAATT-3′) were ordered from GenePharma. Transfection of cells with siRNAs was performed using Lipofectamine RNAiMAX transfection reagent (Invitrogen, 13778-075) according to the manufacturer's protocol. Briefly, 25 pmol siRNA was mixed with 7.5 μl Lipofectamine RNAiMAX in Opti-MEM medium and incubated for 5 min before the mixture was added to the cells.

Immunofluorescence staining and live-cell imaging. Cells were passaged into a 35 mm Petri dish, fixed with 4% paraformaldehyde in PBS for 10 min, blocked in buffer containing 10% BSA and 0.5% Triton X-100 in PBS for 1 h, and then incubated with primary antibodies for 2 h at RT. The cells were then washed three times with PBS and incubated with Alexa Fluor 488/647/Cy3B-conjugated secondary antibodies (Thermo Fisher Scientific) for 1 h at RT. Immunofluorescence was detected using a Zeiss LSM 880 confocal microscope. HSF1 primary antibodies (CST, D3L8I, rabbit monoclonal antibody no. 12972; 1:200 dilution), goat anti–mouse IgG(H + L) secondary antibody–Alexa Fluor 647/Cy3B (Thermo Fisher Scientific, A-21240; 1:100 dilution), rabbit IgG (H + L) cross-adsorbed secondary antibody–Alexa Fluor 647/Cy3B (Thermo Fisher Scientific, A-21244; 1:100 dilution), recombinant anti-Brd4 [EPR5150(2)] (Abcam, ab128874; 1:150 dilution), recombinant anti-cyclin T1 (EPR17982) (Abcam, ab184703; 1:100 dilution), recombinant anti-RNA polymerase II CTD repeat YSPTSPS (phospho S5) (EPR19015) (Abcam, ab193467; 1:100 dilution), recombinant anti-RNA polymerase II CTD repeat YSPTSPS (phospho S2) (EPR18855-87) (chromatin immunoprecipitation (ChIP) grade; Abcam, ab238146; 1:100 dilution), anti-histone H3K9 (ChIP grade; Abcam, ab8898; 1:200 dilution) and anti-histone H3K4 (ChIP grade; Abcam, ab8580; 1:200 dilution) were used for immunofluorescence.

HeLa cells transfected with the HSF1–EGFP construct were passaged into a 35 mm Petri dish and imaged using a Nikon Spinning Disk confocal microscope. During image acquisition, the cells were incubated at 37 °C with 5% CO_2. The images were processed and analysed using the ImageJ (National Institutes of Health) and Imaris 9.02 (Oxford Instruments) software. The ImageJ plugin 'coloc2' was used for Pearson's correlation coefficient analysis and the 'Analyze Particle' module was used to identify droplets and calculate the mean intensity of the droplets. The 'Colc' module of Imaris was used to calculate Manders' coefficient.

STORM imaging and data analysis. Super-resolution images of Alexa Fluor 647/Cy3B-labelled HSF1, RPB1, BRD4, H3K9, H3K4 and CYCT1 were acquired continuously for up to 100,000 frames under excitation by a 647 or 561 nm laser (MPB Communications) at a power density of 3–5 kW cm^{-2} and photoactivated with a 405 nm laser (Coherent) at a power density of 0.5 kW cm^{-2}. To correct for lateral drift between frames, bright-field images of 3 μm glass beads (Weike Tech) placed in the sample dish before imaging were acquired every 3,000 ms for 300 ms. An imaging buffer (100 mM Tris–HCl at pH 8.0, 20 mM NaCl and 10% glucose; all from Sigma-Aldrich) and an oxygen-scavenger system (60 mg ml^{-1} glucose oxidase and 6 mg ml^{-1} catalase; both from Sigma-Aldrich) were used for all STORM imaging experiments.

STORM image analysis, drift correction and image rendering were performed using Insight3 (a gift from B. Huang, UCSF), custom-written code in MATLAB (2020a; MathWorks), SR-Tesseler[50] (Interdisciplinary Institute for Neuroscience) and ImageJ. Insight3 was used to find the position of every individual molecule using Gaussian fitting and then the custom MATLAB code was used for drift correction. Briefly, the position of the SiO_2 bead was extracted from the bright-field images. The drift curve was constructed using the position of the beads and used for cross-correlation of the coordinates of every molecule. Image reconstruction was performed using the centroid of each molecule with Gaussian convolution in MATLAB. The custom-written code is available on request. For HSF1-cluster identification, a density factor of two was applied to identify molecules within the cluster using the default parameter in SR-Tesseler. The coordinates of the HSF1 single-molecule localizations were outputted to MATLAB for further analysis and image reconstruction. The intensity heterogeneity index was calculated using the s.d. of all pixels in the images divided by the mean intensity of all pixels (Fig. 7h).

CRISPR–Cas9-mediated knockout and HaloTag insertion into HSF1. HeLa S6 cells with an endogenous C-terminal HaloTag insertion in the HSF1 gene locus were generated using the clustered regularly interspaced short palindromic repeats (CRISPR)–CRISPR associated protein 9 (Cas9) system. The cells were transfected with px330 (1 μg each), which contains single guide RNA (sgRNA) targeting the C terminus of HSF1, and a homology-directed repair template (HSF1 left arm-HaloTag-HSF1 right arm, 500–1,000 bp; 1 μg). Three sgRNA sequences were generated using the online CRISPR design tool and then cloned into the px330 vector (Addgene plasmid no. 42230) using Golden Gate cloning (Bpil). All three sgRNAs (5′-GCCCAGCTCCTCCGGGGCCTCT-3′, 5′-GGGGCCTCTAGGAGACAGTG-3′ and 5′-GCCACTGTCTCCTAGAGG CCC-3′) were transfected as a cocktail using Lipofectamine 3000 transfection reagent (Thermo Fisher Scientific). Both the left and right homologous sequences of HSF1 were amplified using the genome from HeLa cells as the template. Silent mutations were also introduced into the repair plasmid to avoid potential degradation. The cells were incubated at 37 °C for 24 h and then sorted via FACS to isolate single cells expressing the HaloTag insertion for imaging. After two weeks, single-colony expansion was verified using western blots.

For the knockout experiment, four sgRNA sequences (5′-GTATGTCTTCA CTCTTCAGGG-3′, 5′-GTGAAGACATAAAGATCCGCC-3′, 5′-GCTTGGTG ACGCTGTCCTGG-3′ and 5′-GCAGCTTGGTGACGCTGTCC-3′) targeting the N-terminal exons were used.

Recombinant protein expression in *E. coli* BL21 (DE3) cells. Plasmids containing genes tagged with His–EGFP, His–mCh or His–mCardinal were transformed and expressed in *E. coli* BL21 (DE3) cells (Transgene, CD601-01) in Luria–Bertani medium with 50 mg l^{-1} kanamycin. The culture was cooled to 19 °C when it reached an optical density of approximately 0.6–0.8 at 600 nm. Isopropyl β-D-1-thiogalactopyranoside (0.5 mM) was added for 18–20 h to induce protein expression. The cells were harvested by centrifugation at 6,200*g* for 15 min and then resuspended in Buffer A (20 mM HEPES, 1 M NaCl, 30 mM imidazole, 10% glycerol, 1 mM dithiothreitol (DTT) and 20 mM phenylmethylsulfonyl fluoride (PMSF), pH 7.4). The cell suspension was snap-frozen and stored at −80 °C for further protein purification.

Recombinant protein expression in HEK293F suspension cells. HEK293F suspension-adapted cells were cultured according to standard protocols. Briefly, HEK293F cells were cultured in conical cell-culture flasks in an orbital shaker incubator (37 °C, 120 r.p.m. and 5% CO_2) until they reached a density of 1.0×10^6 cells ml^{-1}. Next, the HEK293F cells (1 l) were transiently transfected with HSF1–mCh–6×His (1 mg) using a branched version of polyethyleneimine (1 mg ml^{-1}; 2 ml) according to standard protocols. Following transfection, the cells were incubated in an orbital shaker incubator for another 48 h (37 °C, 120 r.p.m. and 5% CO_2). The culture was incubated for 1 h (42 °C, 120 r.p.m. and 5% CO_2) for HS treatment, while another flask was maintained for 1 h (37 °C, 120 r.p.m. and 5% CO_2) as a control. The HEK293F cells were harvested by centrifugation at 3,000*g* for 5 min, after which the cells were resuspended in Buffer A. The cell suspension was snap-frozen and stored at −80 °C for further protein purification.

Recombinant protein purification. All purification steps were performed at 4 °C to maintain protein activity. Frozen suspensions were quickly thawed in water and lysed by sonication on ice (300 W for approximately 0.5 h). The cell suspension was centrifuged (25,000*g* for 1 h at 4 °C) and filtered through a 0.22 μm syringe filter to obtain soluble material. A HisSep Ni-NTA 6FF chromatography column was balanced with five column volumes of Buffer A. Following filtration, the clarified extract was applied to a 5 ml HisSep Ni-NTA 6FF chromatography column in Buffer A. The column was continually washed using Buffer A to remove non-specific proteins. The 6×His-tagged proteins were then eluted using a linear gradient (10, 20, 40 and 100%) of nickel elution Buffer B (20 mM HEPES, 1 M NaCl, 500 mM imidazole, 10% glycerol, 1 mM DTT and 20 mM PMSF, pH 7.4). The flow-through fractions with the highest peak values were analysed by SDS–PAGE and Coomassie staining. After analysis, the proteins of interest were concentrated and exchanged with Buffer C (20 mM HEPES, 1 M NaCl, 10% glycerol, 1 mM DTT and 20 mM PMSF, pH 7.4) using an Amicon Ultra centrifugal filter unit with a molecular-weight cutoff of 30 kDa . The sample was applied to a Superdex 75 gel filtration column (GE Healthcare) pre-equilibrated in Buffer C. Peak fractions containing the protein of interest were analysed by SDS–PAGE and Coomassie staining. The proteins were pooled and concentrated using an Amicon Ultra 15 ml centrifugal concentrator with a molecular-weight cutoff of 30 kDa. The protein concentration was measured using a Pierce rapid gold BCA protein assay kit (Thermo, A53225). Finally, the proteins were flash-frozen in liquid nitrogen and stored at −80 °C.

In vitro phase separation and fluorescence microscopy imaging. Droplet formation was monitored by differential-interference-contrast and fluorescence microscopy. Protein was added to the phase separation buffer (20 mM HEPES, 200 mM NaCl, 4 mM $MgCl_2$, 20 μM $ZnCl_2$, 1 mM DTT and 10% T500 dextran (Pharmacosmos), pH 7.4) to induce phase separation. To guarantee accuracy, all of the HSF1 was diluted to a final concentration of 4 μM with phase separation buffer containing 200 mM NaCl, unless otherwise indicated. Other transcription apparatuses or chaperones were diluted to an appropriate protein concentration as indicated in the figure or figure legend. All preparation steps were performed at 4 °C to maintain protein activity. The phase-separation mixtures were then balanced at RT for 20 min. A 5–10 μl aliquot of each sample was loaded onto a custom-made glass slide, covered with a coverslip with a diameter of 18 mm and incubated at RT for 20 min before imaging.

Differential-interference-contrast and fluorescence images were acquired on an LSM 880 microscope with a ×100 objective and processed using the ZEN (Zeiss) and Fiji (National Institutes of Health) software. Hundreds of droplets were identified in more than five independent fields of view in each group. To minimize the effects of the interaction between the droplets and the glass surface, the last layer of droplets was avoided when acquiring the images.

For the co-phase separation assay for multiple proteins, all proteins were premixed and then added to the phase separation buffer. The genome sequence used for phase separation of HSF1 and endogenous DNA are as follows (GRCh38 primary assembly): *HSP90AB1*, chr6:44247619–44248623; *HSPA1A*, chr6:31814581–31815585; *HSPA6,* chr1:161522786–161526794 and *HSPH1*, chr13:31157789–31162268.

The partition coefficient (ratio) was calculated as $x = \frac{I_{den}}{I_{dil}}$, where I_{den} is the intensity of the dense phase and I_{dil} is the intensity of the dilute phase.

FRAP assay. All FRAP assays were performed on a Zeiss LSM 880 confocal microscope. Each fluorescent protein signal was bleached using its specific stimulated laser beam. We used an unbleached region to correct the bleached region. To reduce the phototoxic effect, all laser lines were set to a transmission of less than 20% for the acquisition of the post-bleach images. In one cell, two round bleach regions, each covering one droplet, were chosen to be photobleached. After three pre-bleach frames with a time interval of 200 ms, 40 post-bleach frames were recorded with a time interval of 5 s. The pre-bleaching fluorescence intensity was normalized to one.

In vitro kinase assay. CK II (New England Biolabs, P6010L) was incubated with HSF1–mCh (purified from *E. coli*) according to standard protocols. Briefly, 20 μg of HSF1–mCh protein purified from *E. coli* was mixed with 5 μl CK II phosphatase in reaction buffer (20 mM Tris–HCl, 50 mM KCl, 10 mM $MgCl_2$ and 200 μM ATP, pH 7.5) and incubated at 30 °C for 30 min. For the in vitro droplet-formation assay, the mixture was subjected to the phase-separation assay.

DNA and RNA FISH with immunofluorescence. Petri dishes (30 mm) were coated with 5 μg ml^{-1} poly-L-ornithine (Sigma-Aldrich, P4957) for 2 h and washed three times with PBS. Cells were plated on pre-coated coverslips and cultured for 24 h, followed by fixation using 4% paraformaldehyde (VWR, BT140770) in PBS for 15 min. Next, the fixed cells were washed three times in PBS, permeabilized using 0.5% Triton X-100 (Sigma-Aldrich) in PBS for 10 min and blocked with 10% BSA (Yeasen, 36101ES25) for 30 min. The cells were incubated with a primary antibody to HSF1 (CST, D3L8I, rabbit monoclonal antibody no. 12972; 1:200 dilution) in PBS for 2 h at RT, washed three times with PBS and incubated with secondary antibodies (Thermo Fisher Scientific; goat anti–mouse IgG1 secondary antibody, Alexa Fluor 647/Cy3B; 1:100 dilution) in PBS for 1 h at RT. Finally, the cells were washed three times with PBS and post-fixed using 4% paraformaldehyde in PBS for 15 min.

For RNA FISH, we used a Cy3-labelled secondary probe coupled with unlabelled primary probes[51]. We designed 47 primary probes (Supplementary Table 2) covering the coding region of HSP70 (*HSPA1L*). Hybridization of the primary probe set with the secondary probe (5′Cy3-CACTGAGTCCAGCTCGAAACTTAGGAGG-3′) was performed in NEB3.1 Buffer in a PCR machine (85 °C for 3 min, 65 °C for 3 min and 25 °C for 5 min). Cells were permeabilized in 70% ethanol at 4 °C overnight with a Parafilm sheet wrapped around the dishes. Next, the cells were rinsed once with PBS and incubated in 15% formamide freshly prepared in 1×saline-sodium citrate (SSC) buffer (Ambion, AM9763) for 15 min at RT. A 200 μl reaction mixture containing 10 μl of 20×SSC, 4 μl of 20 μg μl^{-1} *E. coli* transfer RNA, 30 μl of 100% formamide, 4 μl of annealed probes, 2 μl of 20 mg ml^{-1} RNase-free BSA, 2 μl of 200 mM VRC, 53 μl of 40% dextran sulphate and 96 μl DEPC-treated water was prepared on ice. The PBS was removed from the dishes and the reaction mixture was added to the cells. The Petri dish was wrapped with parafilm and incubated overnight at 37 °C in a humidified incubator. The hybridization mixture was removed on the second day and the cells were washed using freshly prepared 15% formamide in 1×SSC at 37 °C for 30 min, after which the cells were rinsed twice in PBS.

For DNA FISH, we used Oligopaint with secondary probe labelling. The primary probe sets were generated by array-based oligo library synthesis (Synbio Technologies), followed by high-yield enzymatic amplification using T7 in vitro transcription and reverse transcription. The primary probe sets are listed in Supplementary Table 3. Before the FISH was performed, the cells were incubated sequentially in 70, 85 and 100% ethanol (1 min each) at RT. Next, the cells were permeabilized with 0.5% vol/vol Triton X-100 (Sigma, T8787) in PBS for 10 min at RT, washed with PBS for 2 min, treated with 0.1 M HCl for 10 min at RT, washed with PBS twice and digested with 0.1 mg ml^{-1} RNase A in PBS for 45 min at 37 °C. The cells were then washed twice in 1×SSC and incubated for 30 min at RT in pre-hybridization buffer containing 2×SSC, 50% formamide (Ambion, AM9342) and 0.1% vol/vol Tween 20 (Fisher, BP337). For hybridization, 200 μl hybridization buffer consisting of 2×SSC, 50% formamide, 20% dextran sulfate (Sigma, D8906-50G) and the primary probe sets (10 μM) was added to the cells. The cells were placed on a heating block at 86 °C for 5 min to denature the chromosomal DNA, after which the sample was incubated overnight in a humid chamber at 37 °C. The samples were washed twice with 2×SSC + 0.1% vol/vol Tween 20 at 60 °C (15 min each wash), followed by an additional wash in the same mixture at RT for 15 min. Finally, the samples were washed in 2×SSC buffer for 15 min. Images were acquired using a custom microscope with a ×100 objective. The images were post-processed using Fiji (ImageJ) and MATLAB.

Nascent RNA labelling. For nascent RNA labelling, 5-ethynyl uridine was fed to cells and allowed to actively incorporate into nascent RNA for 20 min in a 37 °C incubator. Next, 1 ml of 4% formaldehyde in PBS was added to each well and the cells were incubated at RT for 15 min, after which 0.5% vol/vol Triton X-100 in PBS was used to penetrate the cells for 15 min at RT. Chemoselective ligation was utilized to detect nascent RNA through a 'click' reaction between an alkyne and Alexa Fluor 488 or Alexa Fluor 647 azide for 30 min (Invitrogen, Click-iT RNA imaging kits, cat. no. C10329).

Gal4–mClover reporter assay. The piggy vector (1 μg) containing nine GAL4 upstream activation sites (UAS) upstream of the *mClover3* gene was co-transfected with the PiggyBase vector (250 ng) into HeLa cells using Lipofectamine 3000 (Thermo Fisher, L3000015) in a six-well plate to construct stable cells. One week after transfection, FACS was used to isolate single clones with proper expression of mClover3 into a 96-well plate. After clone expansion for 3 weeks, each single cell clone was digested and transferred to a six-well plate for further expansion for about 1 week. A subset of clones was transferred to a 30 mm glass-bottomed dish for further screening using fluorescence imaging. A single cell clone with mediate and homogeneous expression was chosen for further experiment. The Gal4 DBD was assembled in a mammalian expression vector (pcDNA3.1(+)) containing a CMV promoter to drive its expression. Different HSF1 truncation and mutant constructs were fused to the C terminus of the Gal4 DBD by Gibson assembly (Yeasen, Hieff clone plus multi one step cloning kit, 10912ES10). An mScarlet expression cascade driven by another CMV promoter was also inserted into these HSF1-containing vectors to quantify the expression levels of each HSF1 truncation and mutant. These chimaeric transcription-factor constructs (1 μg each) were then separately transfected into 9×UAS–mClover3 stable cells in a six-well plate using Lipofectamine 3000. The expression levels of mScarlet and mClover3 24 h after transfection were recorded using FACS. The FlowJo (v. 10.5.3) software was used for analysis of the flow cytometric data.

Western blotting. Cells were lysed in RIPA lysis buffer (Beyotime, P0013B) with the protease inhibitor PMSF (Beyotime, ST505). The lysate was run on a 4–20% Tris–acetate gel (Yeasen, precast protein improve gels, 36231ES10) at 70 V for 1 h, after which the voltage was increased to 100 V until the dye front reached the end of the gel. The separated protein sample was wet-transferred to a 0.45 mm polyvinylidene fluoride membrane (Millipore, IPVH00010) in ice-cold transfer buffer (25 mM Tris, 200 mM glycine and 10% methanol) at 200 mA for 2 h at RT. After the transfer, the membrane was blocked with 5% non-fat milk in TBST with shaking for 1 h at RT. The membrane was incubated with anti-HSF1 (CST, D3L8I, rabbit monoclonal antibody cat. no. 12972; 1:1,000 dilution), anti-GAPDH (Proteintech, 1E6D9, mouse monoclonal cat. no. 60004-1-Ig; 1:20,000 dilution), anti-G3BP1 (CST, E9G1M, rabbit monoclonal antibody cat. no. 61559; 1:1,000 dilution) and anti-HA-Tag (C29F4, rabbit monoclonal antibody cat. no. 3724; 1:1,000 dilution) in 5% non-fat milk in TBST, followed by incubation for 2 h at RT. Next, the membrane was washed three times with TBST for 5 min at RT with shaking. The membrane was incubated with secondary antibodies—goat anti–rabbit IgG H&L (HRP) pre-adsorbed (Abcam, ab7090; 1:5,000 dilution) and goat anti–mouse IgG H&L (HRP) pre-adsorbed (Abcam, ab97040; 1:5,000 dilution)—for 1 h at RT and washed three times in TBST for 5 min. Finally, the membranes were covered with ECL substrate (Thermo Scientific, 34080) and imaged using a charge-coupled-device camera. Cells were centrifuged at 21,100*g* to separate the supernatant and pellet in Fig. 1c.

Lentiviral production. HEK293T cells were plated at a density of 5×10^6 per 10 cm dish 24 h before transfection. The cells were transfected using Lipofectamine 3000 (Lifetech) transfection reagent. Briefly, individual lentiviral transfer plasmids (3 μg pLenti-CMV–HSF1 mutant–EGFP), a packaging plasmid (2.6 μg pCMV-dR8.91) and an envelope protein plasmid (0.3 μg pMD2.G; Addgene, cat. no. 12259) were mixed with transfection reagent in Opti-MEM medium (Gibco). The mixture was

incubated for 30 min at RT and added in a drop-wise manner to the HEK293T cells in 10 ml of fresh DMEM medium in a 10 cm dish. The lentiviral particles were harvested by filtering the supernatant through a 0.45 μm filter 48 h post transfection and either used immediately or stored at −80 °C for future use. Stable transformants with EGFP fluorescence were selected using FACS.

Single-molecule tracking. For live-cell single-molecule imaging of HSF1–HaloTag, cells were cultured overnight on a 35 mm Petri dish. The cells were then labelled with Halo-JF549 dye (final concentration of 0.1 nM) for 15 min and washed three times with PBS. After the final wash, the dish was replenished with fresh phenol red-free medium (Lifetech) for imaging. The single-molecule images were taken on a custom Olympus IX83 inverted microscope equipped with a ×100 UPlanSApo, numerical aperture = 1.49, oil-immersion phase objective and an Andor iXon Ultra EMCCD. The microscope stage incubation chamber was maintained at 37 °C with 5% CO_2. A 561 nm laser was used to excite JF549. The laser power was modulated by an acousto-optic tunable filter. In all single-molecule-imaging experiments, we used highly inclined thin illumination and carefully optimized the angle of the inclined light to reduce the background signal in the live-cell tracking experiment. To perform sparse tracking, the cells were pre-bleached with a high-power laser to bleach most of the labelled molecules and the remaining molecules were resolved. We performed time-lapse illumination with a camera exposure time of 10 ms. Single-molecule videos were recorded successively.

All single-molecule imaging data were analysed using the ImageJ plugin Trackmate[52]. Briefly, the Laplacian of Gaussian detector was used for the detection of single HSF1 molecules with an estimated blob diameter of 10 pixels and threshold of 100, using median filter and sub-pixel localization. The simple linear assignment problem tracker was used in the linking process with the following parameters: linking maximum distance, 10 pixels (160 nm per pixel); gap-closing max distance, 10 pixels; and gap-closing maximum frame gap, 2. In addition, the molecular coordinates were extracted using custom R scripts in RStudio. Analysis of the mean square displacement was carried out using custom MATLAB scripts[53].

RNA extraction and RT–qPCR. Approximately 48 h after transfection in a six-well plate with select plasmids, total RNA was extracted using TRIzol (Invitrogen). RT–qPCR was performed using a Hifair III one-step RT–qPCR SYBR Green kit (11143ES50). *GADPH* or *β-actin* were used as an internal reference gene. All primers used in the qPCR step were designed using primer-BLSAT on the NCBI website. Semi-quantitative PCR analysis was performed to assess the data. Briefly, in each group (experimental and control), *GADPH* or *β-actin* and the gene to be examined (sample) were amplified using the corresponding primers in two different tubes with the same total RNA input (1 μg). Four biological replicates were included in each group. We performed one-step RT–qPCR to quantify the expression levels of the genes of interest. The programme is comprised of two reaction profiles. Profile 1 is used to convert RNA to cDNA and Profile 2 is used to conduct qPCR amplification of the gene of interest. For Profile 1, cDNA synthesis is performed by reverse transcriptase using a 10 min synthesis protocol at 42 °C. For Profile 2, Segment 1 consists of incubation at 95 °C for qPCR-enzyme activation and Segment 2 consists of 40 cycles of qPCR amplification.

To quantify the expression levels of the gene of interest, the C_t values of the sample and *GADPH* or *β-actin* were calculated by setting a cutoff for the relative fluorescence intensity. We used the amplification-based threshold algorithm (the default method in the MxPro QPCR software) to determine the C_t value automatically. The change in the RNA expression level was calculated as follows:

$$C_{t,\mathrm{Sample}} - C_{t,GAPDH/\beta\text{-}actin} = \Delta C_t$$

$$\text{Relative sample RNA expression level} = 2^{-\Delta C_t}$$

$$\text{RNA expression level change} = 2^{-\Delta C_t(\text{experimental})}/2^{-\Delta C_t(\text{control})}$$

The following primers were used for RT–qPCR: *HSPA1A*, 5′-AGCTGGAGC AGGTGTGTAAC-3′ and 5′-CAGCAATCTTGGAAAGGCCC-3′; *GAPDH*, 5′-CAGCAATCTTGGAAAGGCCC-3′ and 5′-GGGGAGATTCAGTGTGG TGG-3′; *DNAJB1*, 5′-AAGGCATGGACATTGATGACC-3′ and GGCCAAAG TTCACGTTGGT-3′; *β-actin*, 5′-GCCGACAGGATGCAGAAGGAGATCA-3′ and 5′-AAGCATTTGCGGTGGACGATGGA-3′; and *RBM23*, 5′-TTGGGGTTT CTCACCAGTTC-3′ and 5′-CTGCAGTGCTGCTTTTCTTG-3′.

EMSA for HSF1 and mutants. Two strands of Cy5-labelled HSE-oligonucleotide were premixed and annealed for 10 min. HSF1 and mutant proteins (500 nM) were mixed with 200 nM annealed HSE probe as well as the appropriate concentration of 1,6-hexanediol and incubated for 10 min on ice. After incubation, the samples were incubated at RT for 30 min, mixed with glycerol and loaded onto a pre-chilled 1% agarose gel (TAE) at 4 °C. The agarose gel was run for 30 min at 150 V in a cold room maintained at 4 °C. Labelled HSE-DNA was detected using a FUJI LAS-4000 fluorescence imager (Fuji Photo Film). The following primers were used for EMSA: Cy5-HSE F, 5′-Cy5-CCCCTTCCCGAATATTCCCCC-3′; and HSE R, 5′-GGGGGAATATTCGGGAAGGGG-3′.

Cut&Tag. We performed the Cut&Tag experiments according to the manufacturer's instructions (Vazyme, cat. no. TD901-TD902). HeLa cells were harvested, counted and centrifuged at 600*g* for 3 min at RT. The cells (100,000) were washed twice in 1.5 ml wash buffer (20 mM HEPES pH 7.5, 150 mM NaCl, 0.5 mM spermidine and 1×protease inhibitor cocktail) by gentle pipetting. Concanavalin A beads (10 μl; Bangs Laboratories) were activated and added to each sample. The mixture was rotated and incubated at RT for 15 min. The supernatant was removed and the bead-bound cells were resuspended in 50 μl Dig-wash buffer (20 mM HEPES pH 7.5, 150 mM NaCl, 0.5 mM spermidine, 1×protease inhibitor cocktail and 0.05% digitonin) containing 2 mM EDTA and a 1:50 dilution of the primary antibodies. The mixture was incubated at RT for 2 h with was rotation. The primary antibodies were then removed by removing all of the supernatant after placing the tube on the magnet stand. The secondary antibody (guinea pig anti–rabbit IgG) was diluted 1:50 in 50 μl Dig-Wash buffer and incubated at RT for 30 min. The cells were washed three times (5 min each) in 800 μl Dig-Wash buffer to remove the unbound antibodies. A 1:200 pG-Tn5 adaptor complex (approximately 0.04 μM) was prepared in Dig-300 buffer (0.05% digitonin, 20 mM HEPES, pH 7.5, 300 mM NaCl, 0.5 mM spermidine and 1×protease inhibitor cocktail) and added to the cells. The cells were rotated and incubated with transposase at RT for 1 h. The cells were washed three times (5 min each) in 800 μl Dig-300 buffer to remove unbound pG-Tn5 protein, resuspended in 100 μl Tagmentation buffer (10 mM $MgCl_2$ in Dig-300 buffer) and incubated at 37 °C for 1 h. Next, 10 μl of 0.5 M EDTA, 3 μl of 10% SDS and 2.5 μl of 20 mg ml^{-1} proteinase K were added to the sample, which was incubated at 55 °C for 60 min to stop tagmentation. The total DNA was then extracted using phenol–chloroform–isoamyl alcohol (25:24:1; Invitrogen, cat. no. 15593049). To amplify libraries, 21 μl DNA was mixed with 2 μl of a uniquely barcoded i5 primer and an i7 primer (Vazyme, cat. no. TD202), using a different barcode for each sample. A volume of 25 μl NEBNext HiFi 2×PCR master mix was added and mixed. The sample was amplified in a Thermocycler with a heated lid using the following cycling conditions: 72 °C for 5 min (gap filling), 98 °C for 30 s, 14 cycles of 98 °C for 10 s and 63 °C for 30 s, and final extension at 72 °C for 1 min, followed by a hold at 4 °C. Post PCR clean-up was performed by adding a 1.1×volume of Ampure XP beads (Beckman Counter), and the libraries were incubated with the beads for 10 min at RT, washed twice gently in 80% ethanol and eluted in 23 μl of 10 mM Tris, pH 8.0. The concentration of each sample was measured using an Invitrogen Qubit 4 system. The size distribution of the libraries was determined by fragment-analysis capillary electrophoresis, using 2 μl of sample, following the manufacturer's instructions. Bead selection to choose DNA fragment sizes of between 300 and 500 bp using Ampure XP beads was performed. The library was pooled with an equal number of moles and paired-end sequencing was performed on a single lane of an Illumina NovaSeq system yielding paired-end reads of 150 bp. HSF1 primary antibodies (CST, D3L8I, rabbit monoclonal antibody no. 12972; dilution 1:50), recombinant anti-Brd4 (EPR5150(2)) (Abcam, ab128874; 1:100 dilution), recombinant anti-cyclin T1 (EPR17982) (Abcam, ab184703; 1:100 dilution), recombinant anti-RNA polymerase II CTD repeat YSPTSPS (phospho S5) (EPR19015) (Abcam, ab193467; 1:100 dilution), anti-histone H3 (trimethyl K9) (ChIP grade; Abcam, ab8898; 1:50 dilution), anti-histone H3 (trimethyl K4) (ChIP grade; Abcam, ab8580; 1:50 dilution), guinea pig anti–rabbit IgG (heavy and light chain) (Antibodies-Online, ABIN101961; 1:100 dilution) were used for the Cut&Tag.

For the Cut&Tag data analysis, the paired-end reads were aligned to the human genome build GRCh38/hg18 using Subread-align[54]. The SEACR software was used for peak identification with data from IgG1 input as controls and default parameters[55]. The Homer (v. 4.10.0) 'annotatePeaks' and 'find-MotifsGenome' functions were used to annotate the called peaks and find enriched motifs in these called peaks[56]. Alignment files in the bam format were also transformed into read coverage files (bigwig format) using DeepTools[57] for visualization in Integrative Genome Viewer[58]. Genomic binding profiles were generated using the deepTools 'bamCompare' functions. Heat maps for ChIP-seq signals were generated using the deepTools 'computeMatrix' and 'plotHeatmap' functions.

RNA-seq. TRIzol reagent (Invitrogen) was used to isolate total RNA from HeLa cells, and the VAHTS universal V8 RNA-seq library prep kit for Illumina (Vazyme, cat. no. NR605) and KAPA HyperPrep kit (Roche, cat. no. KR0961) were used to prepare the cDNA libraries. Briefly, 1 μg total RNA was diluted with ddH_2O to a final volume of 50 μl. Activated RNA capture beads (50 μl) were added to the RNA samples and mixed thoroughly. The mixture was heated to 65 °C for 5 min and then cooled to 4 °C. The samples were incubated at RT for 5 min to allow the mRNA to bind to the beads. A magnetic rack was then used to isolate and purify the mRNA. A 11.5 μl volume of the Frag/Prime Buffer and random primer mix were added to elute the mRNA from the beads. The samples were heated for 8 min at 94 °C in a thermocycler, followed by a hold at 4 °C. The tube was spun briefly in a microcentrifuge to collect the liquid from the sides of the tube, immediately placed on the magnet and left for 5 min to allow the solution to become clear. The fragmented mRNA was collected by transferring 10 μl of the supernatant to a nuclease-free 0.2 ml PCR tube. A mix of 10 μl fragmented mRNA, 8 μl nuclease-free water and 2 μl first-strand synthesis enzyme mix was placed in a thermocycler for first-strand cDNA synthesis (25 °C for 10 min, 42 °C for 15 min, 70 °C for 15 min

and hold at 4 °C). The second strand cDNA synthesis reaction was assembled as follows: 20 µl first-strand cDNA, 8 µl reaction buffer, 4 µl second strand enzyme super mix 2 and 48 µl nuclease-free water. The mixture was thoroughly mixed by pipetting the reaction up and down and then incubated in a thermocycler for 1 h at 16 °C. The cDNA was purified using SPRIselect beads and eluted in 50 µl TE buffer. Next, 50 µl cDNA, 7 µl reaction buffer and 3 µl enzyme mix were mixed and incubated in a thermocycler (20 °C for 30 min, 65 °C for 30 min and hold at 4 °C). A ligation reaction was assembled on ice (60 µl of the end-prepared DNA, 2.5 µl diluted adaptor, 1 µl ligation enhancer and 30 µl ligation master mix), incubated for 15 min at 20 °C in a thermocycler, followed by the addition of 3 µl USER enzyme and incubation at 37 °C for 15 min. Purification of the ligation reaction was performed using SPRIselect beads. We then performed PCR enrichment of the adaptor-ligated DNA with the following reaction set-up: 15 µl adaptor-ligated DNA, 25 µl Master Mix and 5 µl i5/i7 primers. Amplification was performed in a thermocycler with a heated lid using the following cycling conditions: 98 °C for 30 s, 12 cycles of 98 °C for 10 s and 65 °C for 95 s, final extension at 65 °C for 5 min and hold at 4 °C. The PCR reaction was purified using SPRIselect beads. Quantitative PCR was used to measure the concentration of each sample and fragment-analysis capillary electrophoresis was used to determine the size distribution of the libraries. A bead selection using Ampure XP beads was run to select DNA fragment sizes of 300–500 bp. The library was pooled together with an equal number of moles and paired-end sequencing was performed on a single lane of an Illumina NovaSeq system yielding paired-end reads of 150 bp.

For the RNA-seq data analysis, the paired-end reads were aligned to the human genome build GRCh38/hg18 using Subread-align[54]. Only uniquely mapped reads were retained for further analysis. The number of read counts for each gene was calculated using Subread -featureCounts. For each library, the read counts were adjusted using the iDEP web tool[59]. Regularized-log transformation implemented in the DESeq2 package[60] was used to transform the data, as it effectively reduces the mean-dependent variance. Differential expression analysis of two groups was performed using the DESeq2 package. The *P* values were adjusted using the Benjamini–Hochberg method. Genes with an adjusted $P < 0.005$ and absolute $\log_2$(fold change) > 1 were considered as significantly differentially expressed genes.

Statistics and reproducibility. All experiments were performed at least three times independently with similar results, unless otherwise indicated in the figure legends. No statistical method was used to pre-determine the sample size. No data were excluded from the analyses. Statistical analyses were performed using the 't.test' function in R. Data are presented as the mean ± s.d. All statistical tests were two-sided and a *P* value of less than 0.05 was considered statistically significant. An unpaired two-sided Student's *t*-test was used to compare the size and droplet numbers in the in vitro and qPCR experiments. The analysis (two-sided) of differentially expressed genes was conducted using Deseq2 and the *P* values were adjusted for multiple comparisons using the Benjamini–Hochberg correction. Enriched pathways were generated by gene-set enrichment analysis and the *P* values were adjusted for multiple comparisons using the Benjamini–Hochberg correction. All boxes in the boxplots extend from the 25th to the 75th percentiles; the line in the box represents the median and the whiskers represent the range within 1.5× the interquartile range. Minima and maxima are not shown.

Reporting Summary. Further information on research design is available in the Nature Research Reporting Summary linked to this article.

Data availability

All of the data associated with the figures are provided as Supplementary Information. The human genome GRCh38/hg18 was used for the alignment of the Cut&Tag and RNA-seq dataset. The Cut&Tag and RNA-seq datasets generated in this study have been deposited to NCBI Gene Expression Omnibus under the accession numbers GSE192370 and GSE191134. All other data supporting the findings of this study are available from the corresponding authors on reasonable request. Source data are provided with this paper.

Code availability

Code for the analysis of STORM data has been deposited to Zenodo (https://zenodo.org/record/5804854#.YcgnNmjP0uU).

References

50. Levet, F. et al. SR-Tesseler: a method to segment and quantify localization-based super-resolution microscopy data. *Nat. Methods* **12**, 1065–1071 (2015).
51. Tsanov, N. et al. smiFISH and FISH-quant—a flexible single RNA detection approach with super-resolution capability. *Nucleic Acids Res.* **44**, e165 (2016).
52. Tinevez, J.-Y. et al. TrackMate: an open and extensible platform for single-particle tracking. *Methods* **115**, 80–90 (2017).
53. Shao, S. et al. Long-term dual-color tracking of genomic loci by modified sgRNAs of the CRISPR/Cas9 system. *Nucleic Acids Res.* **44**, e86 (2016).
54. Liao, Y., Smyth, G. K. & Shi, W. The Subread aligner: fast, accurate and scalable read mapping by seed-and-vote. *Nucleic Acids Res.* **41**, e108 (2013).
55. Meers, M. P., Tenenbaum, D. & Henikoff, S. Peak calling by sparse enrichment analysis for CUT&RUN chromatin profiling. *Epigenetics Chromatin* **12**, 42 (2019).
56. Heinz, S. et al. Simple combinations of lineage-determining transcription factors prime cis-regulatory elements required for macrophage and B cell identities. *Mol. Cell* **38**, 576–589 (2010).
57. Ramirez, F. et al. deepTools2: a next generation web server for deep-sequencing data analysis. *Nucleic Acids Res.* **44**, W160–W165 (2016).
58. Robinson, J. T. et al. Integrative genomics viewer. *Nat. Biotechnol.* **29**, 24–26 (2011).
59. Ge, S. X., Son, E. W. & Yao, R. iDEP: an integrated web application for differential expression and pathway analysis of RNA-Seq data. *BMC Bioinform.* **19**, 534 (2018).
60. Love, M. I., Huber, W. & Anders, S. Moderated estimation of fold change and dispersion for RNA-seq data with DESeq2. *Genome Biol.* **15**, 550 (2014).

Acknowledgements

We thank L. D. Lavis (HHMI, Janelia Research Campus) for providing the HaloTag ligand dyes JF549 and 646 (Janelia Fluor 549, 646) as well as T. Czerny and E. Riegel (University of Navarre) for providing us with the 6×HSE plasmid. We thank the National Center for Protein Sciences at Peking University in Beijing, China, for assistance with the microscopy imaging, flow cytometry and protein preparation. This work was supported by grants from the National Science Foundation of China (grant nos 21825401 (Y.S.), 31900898 (S.P.) and 82070301 (Y.Z.)), the China Postdoctoral Science Foundation (S.P.; grant nos 2019M660004 and 2019T120013) and the National Key R&D Program of China (Y.S.; grant no. 2017YFA0505300).

Author contributions

H.Z., S.S. and Y.S. conceived and designed the experiments. H.Z. performed most of the experiments. S.S. performed the live-cell and STORM imaging. X.W. assisted with the identification of the IDR of HSF1. Y.Q. helped with the STORM imaging. Q.R. and S.X. performed the NMR experiments. Y.W. and J.X. helped with protein purification from HEK293F cells. H.Z. and S.S. analysed all of the data. H.Z., S.S., Y.Z. and Y.S. wrote the manuscript.

Competing interests

The authors declare no competing interests.

Additional information

Extended data is available for this paper at https://doi.org/10.1038/s41556-022-00846-7.

Supplementary information The online version contains supplementary material available at https://doi.org/10.1038/s41556-022-00846-7.

Correspondence and requests for materials should be addressed to Shipeng Shao or Yujie Sun.

Peer review information *Nature Cell Biology* thanks Bernd Bukau and the other, anonymous, reviewer(s) for their contribution to the peer review of this work.

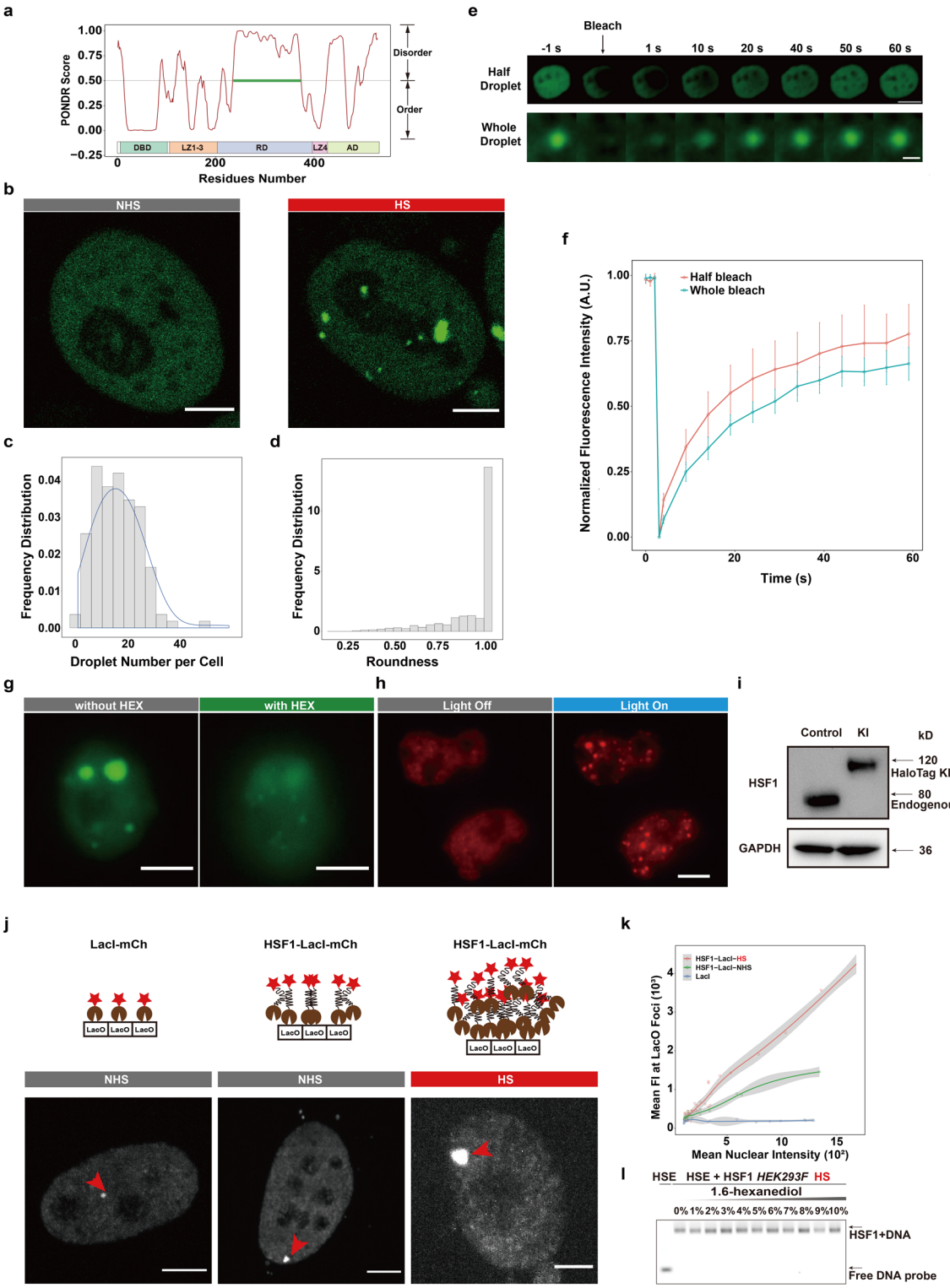

Extended Data Fig. 1 | See next page for caption.

Extended Data Fig. 1 | HSF1 undergoes LLPS during HS. (**a**) Prediction of intrinsically disordered residues in HSF1 protein by Predictor of Natural Disordered Regions (PONDR). The disordered region is shown by a green horizontal line. The domain organizations of HSF1 are shown at the bottom. (**b**) Fluorescence images of HeLa cells transfected with HSF1–EGFP under NHS and HS (42 °C, 0.5 h) conditions. Scale bars, 5 μm. (**c**) Frequency distribution of the number of HSF1 nSBs per cell. 2256 nSBs were analysed in 139 cells pooled across 3 independent experiments. (**d**) Roundness distribution of the HSF1 nSBs. 2256 nSBs were analysed in 139 cells pooled across 3 independent experiments. (**e**,**f**) FRAP recovery of nSBs formed by HSF1. Cells were heat-shocked for 0.5 h at 42 °C to induce phase separation and FRAP was performed after HSF1 droplets emerged. Whole droplets were bleached for the analysis of exchange between nucleoplasm and nSBs, while half droplets were bleached for the analysis of exchange within nSBs and exchange between nucleoplasm and nSBs. Data are presented as mean ± s.d. n = 16 droplets for whole, n = 16 droplets for half collected from 3 independent experiments. Scale bars, 1 μm (e). Fluorescence intensity tracks of the whole droplet and half droplet bleach (f). (**g**) Fluorescence images of HSF1 droplets under HS (42 °C, 0.5 h) condition before and after treatment with 10% 1,6-hexanediol for 1 min. Scale bars, 10 μm. (**h**) Inducing of HSF1 phase separation by Opto-Droplet in living cells under NHS condition. Representative fluorescence images showing the distribution of HSF1 before and after blue light activation. Scale bar, 10 μm. (**i**) Western blot showing slower migration of HSF1–HaloTag in the successful knock-in cells. GAPDH was used as a loading control. (**j**,**k**) Recruitment of HSF1 to LacO array can mediate the formation of a low-complexity domain (LCD) hub in living cells. Top, schematic for a LacO array (~256 LacO repeats) integrated into the genome of NIH3T3 cells. Bottom, HSF1-LacI-mCh formed an LCD hub after HS (42 °C, 0.5 h) when transiently expressed. Alternatively, LacI-mCh and HSF1-LacI-mCh were transiently expressed under NHS condition as controls. Scale bars, 5 μm (j). The mean fluorescence intensity at LacO foci in cells with different expression levels for the LacI-mCh (NHS), HSF1-LacI-mCh (NHS) and HSF1-LacI-mCh (HS) were measured (k). n = 22 cells for LacI, 21 cells for HSF1-LacI-NHS, and 38 cells for HSF1-LacI-HS pooled from 3 independent experiments. The data was smoothed in R using lm() function for linear smooths, and error bands represent the standard error of the smoothing. (**l**) EMSA showing that 1,6-hexanediol does not disrupt HSF1–DNA interaction. Images are representative of three independent experiments (b, e, g-j, l).

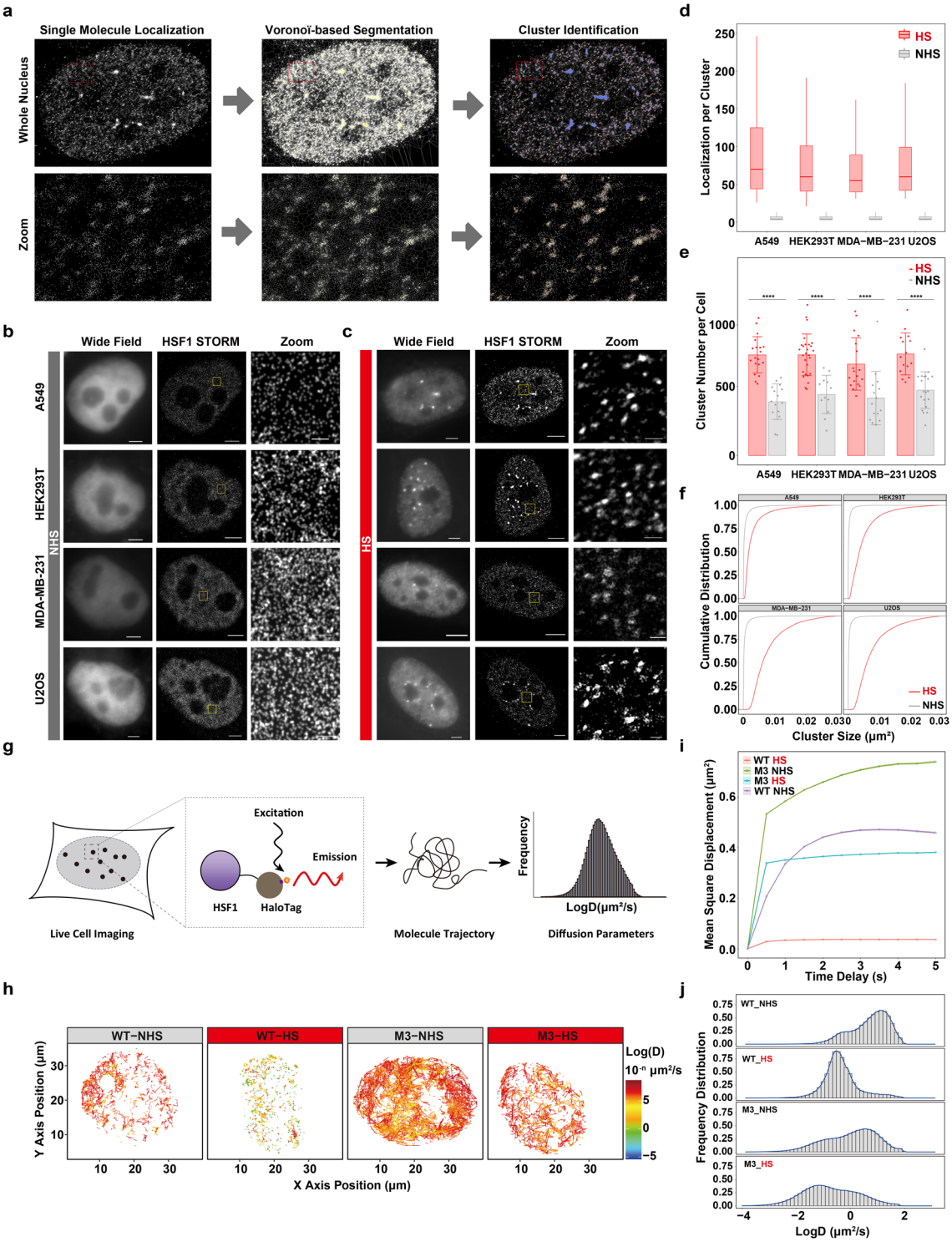

Extended Data Fig. 2 | See next page for caption.

Extended Data Fig. 2 | The formation of small condensates of HSF1 in the nucleoplasm in response to HS. (**a**) Voronoï-based segmentation of HSF1 condensates. Zoomed images were displayed at the bottom. Each molecule has a polygon defined by its neighbouring molecules. Edges of Voronoï polygons are located equidistant from the nearest two molecules. When a new molecule is added, this bisector is cut by the bisectors computed between the old molecules and the new ones. Each new molecule was computed to plot the Voronoï diagram repeatedly until all the molecules were counted. Then a threshold was set twice the average localization density to choose the clusters of HSF1 molecules. (**b**,**c**) Representative fluorescence images of widefield and STORM showing the formation of small condensates in different cell lines under NHS (b) and HS (42 °C, 0.5 h) (c) conditions. Scale bars, 2 μm. Zoomed scale bars, 100 nm. (**d**-**f**) Cluster analysis of HSF1 in different cell lines under NHS and HS (42 °C, 0.5 h) conditions. Localization per cluster (d), cluster number per cell (e), and cluster size (f) were shown. Data are presented as mean ± s.d. Individual data points correspond to the average value for one cell. n = 19 cells for A549-HS, 27 cells for HEK293T-HS, 18 cells for MDA-MB-231-HS, 15 cells for U2OS-HS, 15 cells for A549-NHS, 12 cells for HEK293T-NHS, 15 cells for MDA-MB-231-NHS, 20 cells for U2OS-NHS pooled from 3 independent experiments. The paired two-tailed Student's t-test was used to compare the data (e). Boxplots: 25th to 75th percentiles, median, 1.5×interquartile as whiskers (d). (**g**) Schematic of the single molecule tracking experiment. Using the HaloTag knock-in cells, HSF1 was labelled with JF549 and tracked using HILO illumination. Then the trajectory of each molecule was extracted and analysed. (**h**) The single molecule trajectory of WT HSF1 and LLPS-incompetent M3 under NHS and HS (42 °C, 0.5 h) conditions. The trajectories were colour-coded according to their diffusion coefficients. n = 10 cells for WT HSF1 under NHS, 10 cells for WT HSF1 under HS, 20 cells for M3 under NHS, 16 cells for M3 under HS pooled from 3 independent experiments. (**i**) The mean square displacement of HSF1 and LLPS-incompetent M3 under NHS and HS (42 °C, 0.5 h) conditions. (**j**) The distribution of diffusion coefficient of HSF1 and LLPS-incompetent M3 under NHS and HS (42 °C, 0.5 h) conditions. Images are representative of three independent experiments (b-c).

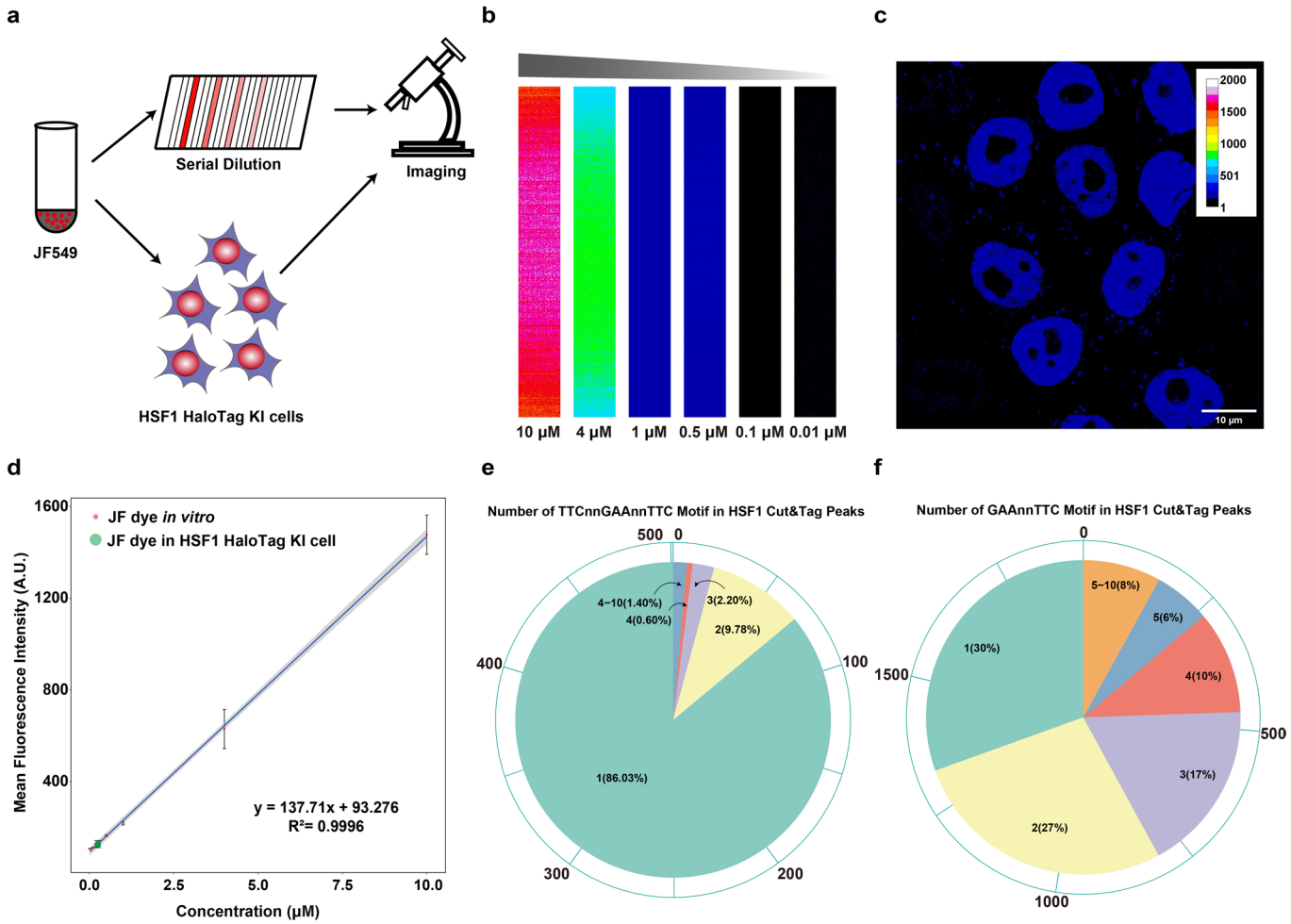

Extended Data Fig. 3 | Measurement of endogenous HSF1 concentration and HSE valency in the promoter of HSP genes. (**a**) Schematic diagram showing the measurement process of HSF1 concentration. A calibration curve was obtained using a serial dilution of JF549 dye to get the relationship between the fluorescence intensity and dye concentration. Under the same imaging condition, JF549 labelled HaloTag knock-in HSF1 cells were imaged to obtain the mean fluorescence intensity of the nucleus. (**b**) Representative images of JF549 dye of different concentrations displayed using the 16 colours lookup table. 9 fields of view were captured to measure the average fluorescence intensity under different concentrations. (**c**) Representative image of HSF1 in HaloTag knock-in cells labelled using JF549 dye. The image was shown using the 16 colours lookup table. Images are representative of three independent experiments. (**d**) Calibration curve between JF549 concentration and fluorescence intensity. Data are displayed as mean ± s.d. n = 9 fields of view pooled from 3 independent experiments. The mean fluorescence intensity of HSF1 in HeLa cells was measured in 501 cells. The ribbon region represents the standard error of the linear fitting. (**e**) Pie plot showing the number of TTCnnGAAnnTTC motif in HSF1 Cut&Tag peaks. (**f**) Pie plot showing the number of GAAnnTTC motif in HSF1 Cut&Tag peaks.

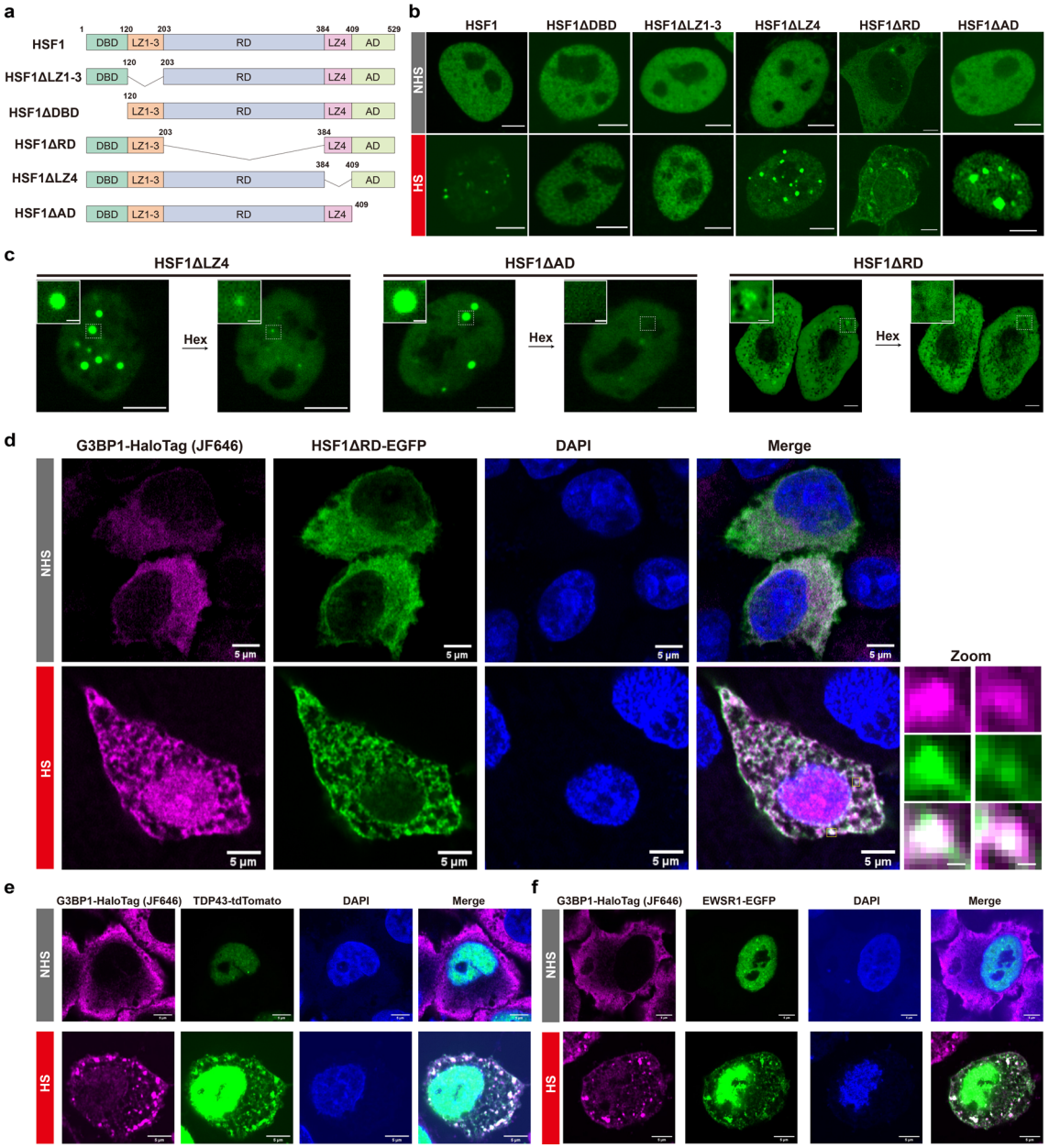

Extended Data Fig. 4 | Both the regulatory and trimerization domains are required for HSF1 phase separation. (**a**) Domain structure of HSF1 truncations. Each amino acid number of the domain boundaries was labelled. (**b**) Confocal microscopy images of HeLa cells transfected with various HSF1 truncations as indicated under NHS and HS (42 °C, 0.5 h) conditions. Scale bars, 5 μm. (**c**) Representative images of HSF1 mutants under HS (42 °C, 0.5 h) condition before and after treatment with 10% 1,6-hexanediol for 1 min. Scale bars, 5 μm. (**d**) Co-localization analysis of HSF1△RD and stress granule marker G3BP1 under NHS and HS (42 °C, 0.5 h) conditions. Scale bars, 5 μm. Zoomed scale bars, 0.5 μm. (**e**,**f**) Co-localization analysis of TDP43 (e) and EWSR1 (f) with stress granule marker G3BP1 under NHS and HS (42 °C, 0.5 h) conditions. Scale bars, 5 μm. All Images in (b-f) are representative of 3 independent experiments.

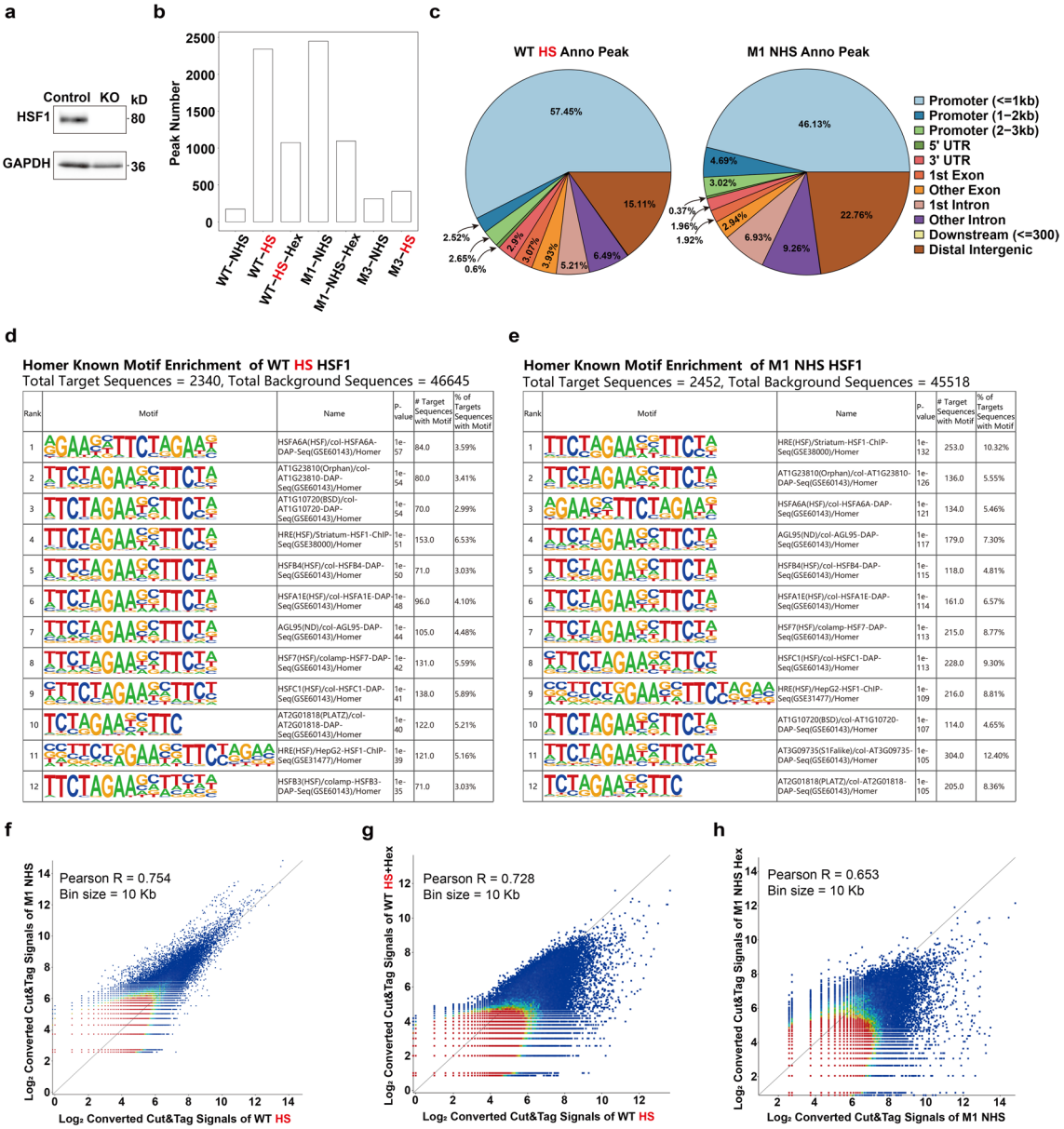

Extended Data Fig. 5 | Cut&Tag reveals similar binding patterns of WT HSF1 under HS and M1 under NHS. (**a**) Western blot showing the successful knockout of HSF1 gene in HeLa cells. Images are representative of 3 independent experiments. (**b**) Peak numbers of Cut&Tag signals under different conditions. (**c**) Pie chart showing the distribution of the indicated annotation feature among the Cut&Tag peaks of WT HSF1 under HS (left) or M1 under NHS (right) condition. (**d**,**e**) Summary of the most enriched motifs identified within the peaks in WT HSF1 under HS (d) and M1 under NHS (e) conditions. Motif enrichment was analysed using Homer and statistically determined by ZOOPS scoring (zero or one occurrence per sequence) coupled with the hypergeometric enrichment calculations. (**f**) Scatterplot showing correlation of global Cut&Tag signal of WT HSF1 under HS and M1 under NHS conditions. The coefficient of determination (R) is determined by two-sided Pearson correlation. The genome was divided into 10 kb bins. (**g**,**h**) The 1,6-hexanediol treatment causes a significant loss of signal in the Cut&Tag experiment. Scatterplot showing correlation of global Cut&Tag signal of WT HSF1 under HS + Hex vs. WT HSF1 under HS (g) or M1 under NHS + Hex vs. M1 under NHS (h) conditions. The coefficient of determination (R) is determined by by two-sided Pearson correlation. The genome was divided into 10 kb bins.

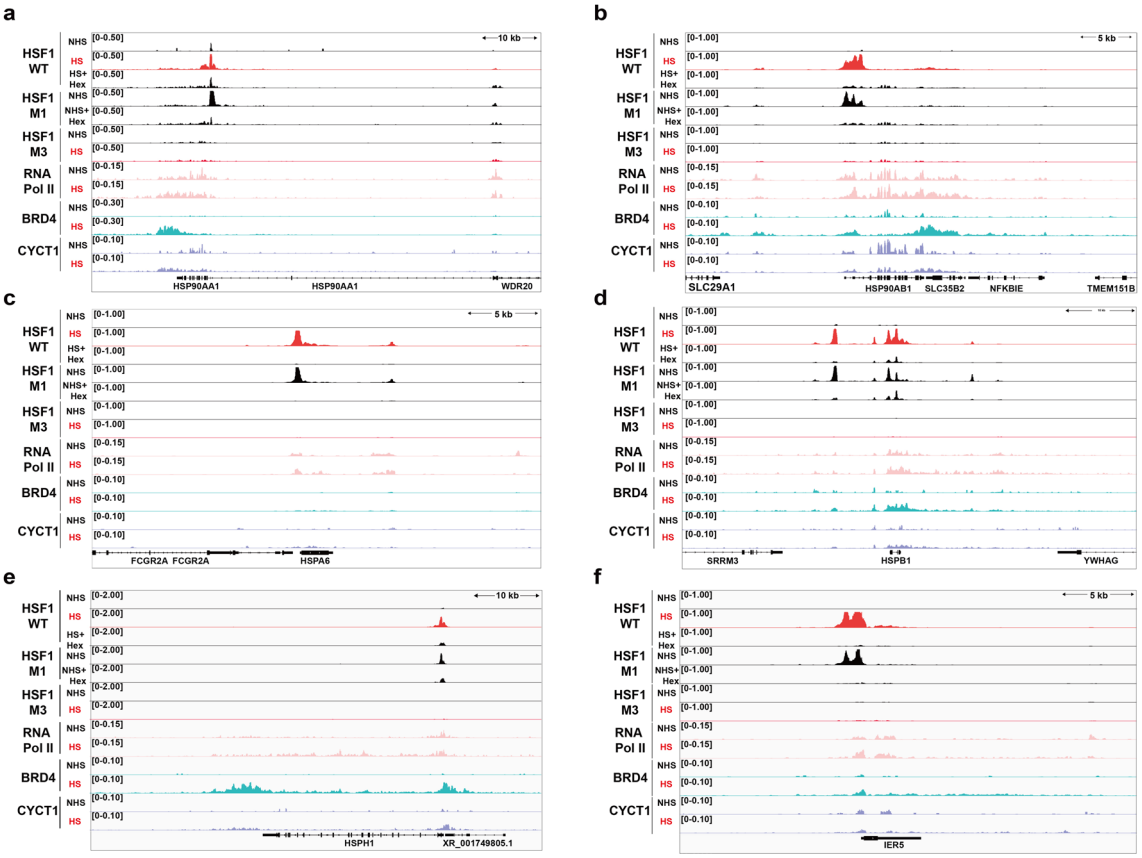

Extended Data Fig. 6 | IGV showing LLPS enhanced chromatin occupancy at multiple HSP gene loci. (**a**-**f**) Integrative genomics viewer (IGV) snapshots for the indicated Cut&Tag signal at the well-known HSP gene foci such as the *HSP90AA1* (a), *HSP90AB1* (b), *HSPA6* (c), *HSPB1* (d), *HSPH1* (e), and *IER5* (f). Samples from top to bottom are HSF1 WT (tracks 1-3), HSF1-M1 (tracks 4-5), HSF1-M3 (tracks 6-7), RNA pol II (tracks 8-9), BRD4 (tracks 10-11), and CYCT1 (tracks 12-13). Tracks 3 and 5 were treated with 1.5% 1,6-hexanediol for 30 mins before Cut&Tag was performed.

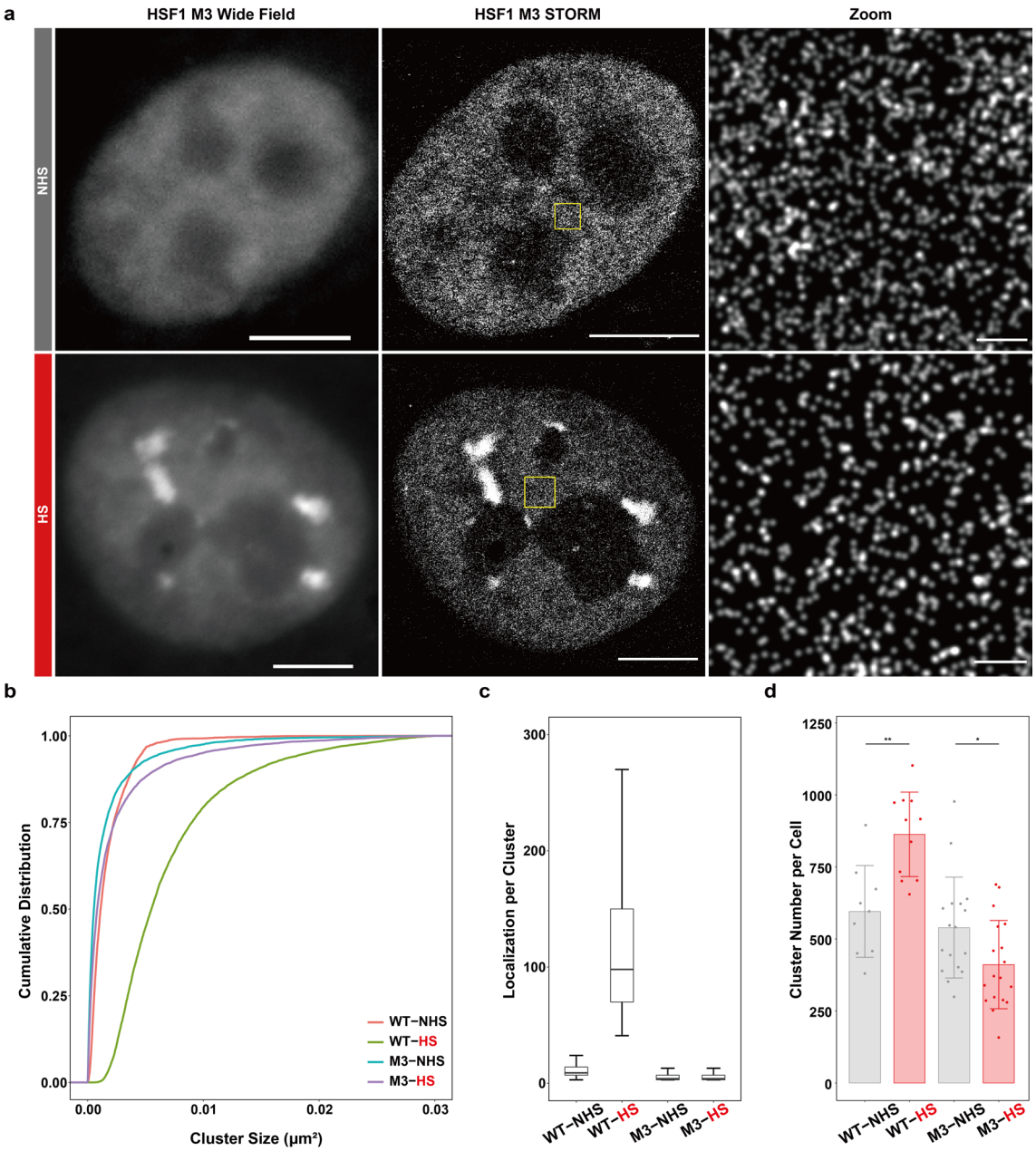

Extended Data Fig. 7 | LLPS-incompetent HSF1 mutant M3 were unable to form small condensates during HS. (**a**) Super-resolution imaging of HSF1 M3 under NHS and HS (42 °C, 0.5 h) conditions. Scale bars, 5 μm. Zoomed scale bars, 0.2 μm. Images are representative of 3 independent experiments. (**b**-**d**) Cluster analysis of HSF1 M3 single molecules under NHS and HS conditions. Individual data points correspond to the average value for one cell. Cluster size (b), localization per cluster (c), and cluster number per cell (d) were shown. Data are presented as mean ± s.d. (d). n = 9 cells of WT NHS, 11 cells of WT HS, 17 cells of M3 NHS, and 18 cells of M3 HS pooled from 3 independent experiments. The paired two-tailed Student's t-test was used to compare the data (d). Boxplots: 25th to 75th percentiles, median, 1.5×interquartile as whiskers (c).

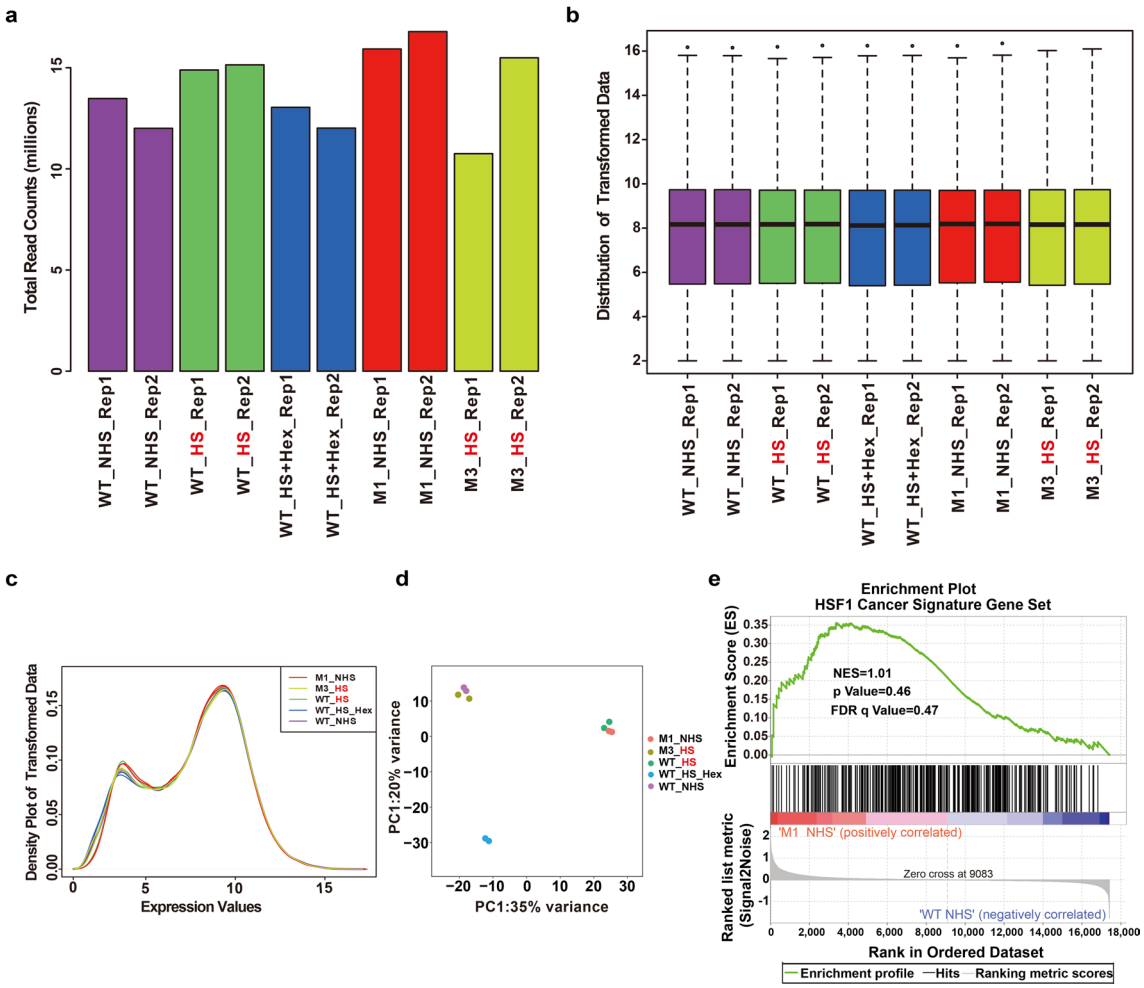

Extended Data Fig. 8 | RNA-seq analysis process of all samples. (**a**) Bar plot showing the total read counts of the RNA-seq libraries. (**b**) Boxplot of transformed data of read counts. The regularized log (rlog) transformation implemented in the DESeq2 package was used to transform the data, as it effectively reduces mean-dependent variance. The transformation was done in the iDEP web tool (http://bioinformatics.sdstate.edu/idep/). Expression profiles of 17683 genes were used to generate the plot. Boxplots: 25th to 75th percentiles, median, 1.5× interquartile as whiskers. (**c**) Density plot showing the read counts vs. the expression level in the transformed data of each library. (**d**) PCA indicated the group of samples. (**e**) Gene set enrichment analysis (GSEA) shows that the differential expressed genes of M1-NHS vs. WT-NHS were not enriched in the cancer-specific target of the HSF1 gene set. The P-value was calculated by an empirical phenotype-based permutation test; the false discovery rate (q) is adjusted for gene set size and several hypotheses testing.

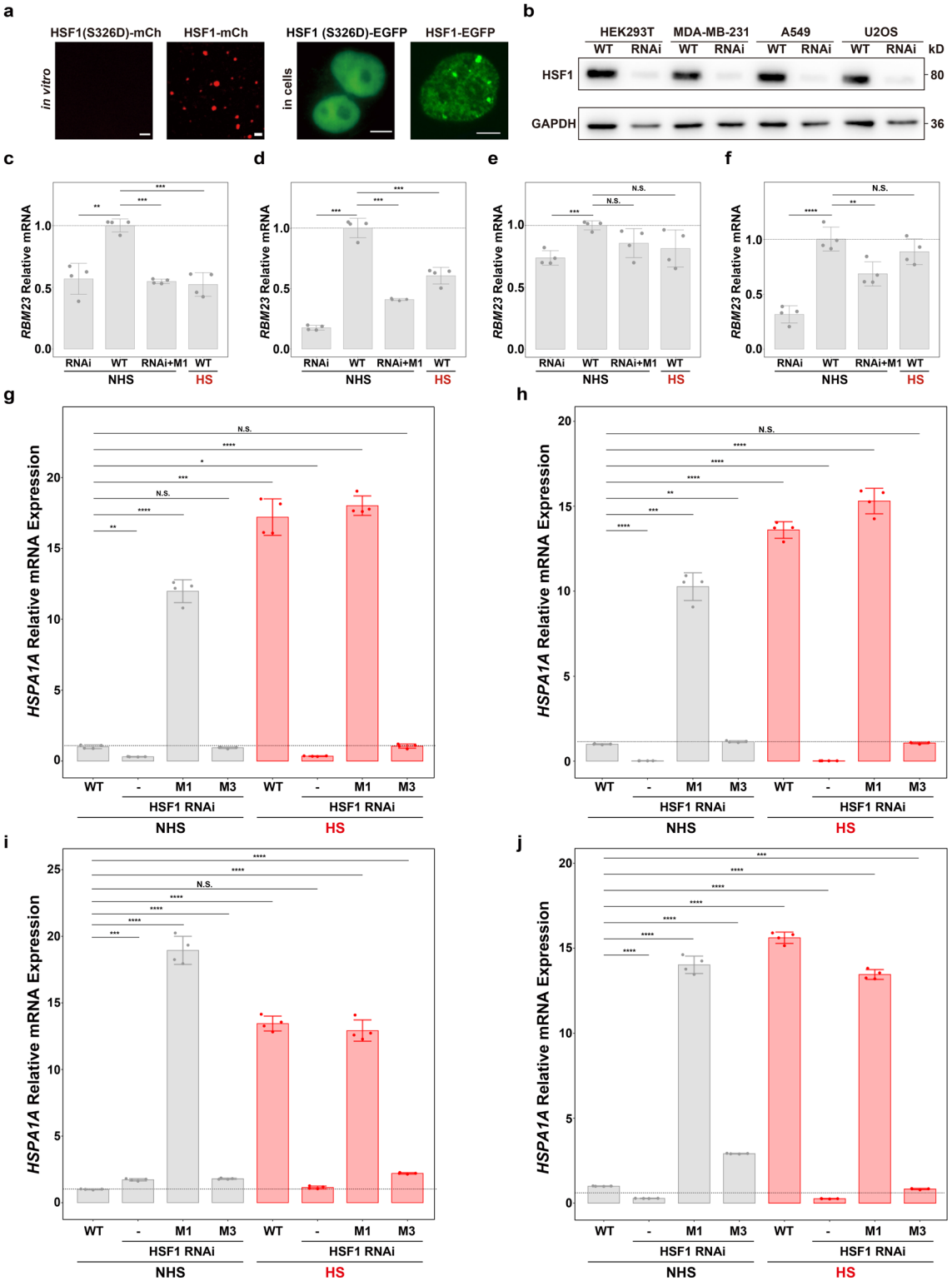

Extended Data Fig. 9 | Phase separation of HSF1 specifically promotes transcription of HSP genes during HS but not cancer-specific genes. (**a**) Left: fluorescence images of HSF1 (S326D) purified from NHS E. coli in the droplet formation assay. HSF1 purified from HS (42 °C, 1 h) human HEK293F cells was used as a positive control. Scale bars, 2 μm. Right: fluorescence images of HSF1 (S326D)-EGFP in HeLa cells under the NHS condition. HSF1-EGFP transfected HaLa cells under HS (42 °C, 0.5 h) were used as a positive control. Scale bars, 5 μm. Images are representative of three independent experiments. (**b**) Western blot showing successful RNAi of HSF1 in HEK293T, MDA-MB-231, A549, and U2OS cells. GAPDH was used as a loading control. Images are representative of three independent experiments. (**c**-**f**) RT-qPCR analysis of *RBM23* mRNA expression in HSF1 RNAi HEK293T (c), MDA-MB-231 (d), A549 (e), and U2OS (f) cells transfected with various HSF1 mutants. Data are presented as mean ± s.d. P-values were determined using a paired two-tailed Student's t-tests. n = 4 biologically independent samples. (**g**-**j**) RT-qPCR analysis of *HSPA1A* (HSP70) mRNA expression in HSF1 RNAi HEK293T (g), MDA-MB-231 (h), A549 (i), and U2OS (j) cells transfected with various HSF1 mutants. Data are presented as mean ± s.d. P-values were determined using a paired two-tailed Student's t-tests. n = 4 biologically independent samples.

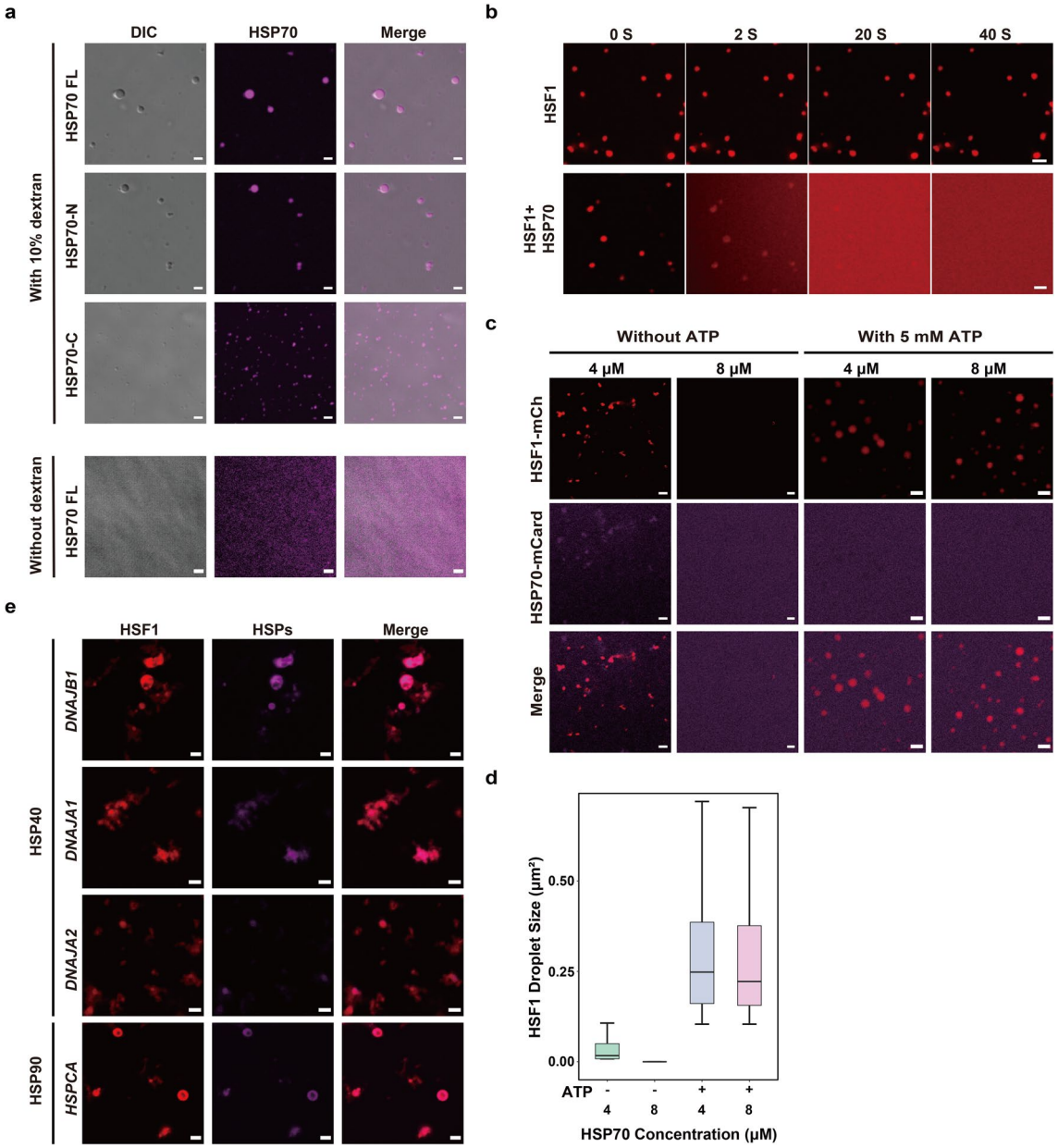

Extended Data Fig. 10 | Negative regulation of HSF1 phase separation during HS is HSP70-specific. (**a**) Representative images of HSP70 FL, HSP70-N, and HSP70-C phase separation. Recombinant HSP70 WT (10 μM), HSP70 N (10 μM), and HSP70 C (10 μM) were added to phase separation buffer with 200 mM NaCl in the presence (top) or absence (bottom) of 10% Dextran-2000. Scale bars, 2 μm. Images are representative of 3 independent experiments. (**b**) HSP70 FL (8 μM) was added to pre-formed HSF1-mCh (4 μM) droplets, the HSF1 droplets were dissolved rapidly *in vitro*. Scale bars, 2 μm. Images are representative of 3 independent experiments. (**c**) Representative images of HSF1-mCh (4 μM) with indicated concentration of HSP70 FL without ATP (left) and with 5 mM ATP (right). Scale bars, 2 μm. Images are representative of 3 independent experiments. (**d**) Analysis of HSF1 droplet size with different HSP70 concentrations (4 μM or 8 μM) with or without ATP. n = 2397/HSF1 + 4 μM HSP70-WO ATP (droplets/group), 0/HSF1 + 8 μM HSP70-WO ATP, 820/HSF1 + 4 μM HSP70-With ATP, 768/HSF1 + 8 μM HSP70-With ATP pooled across 3 independent experiments. Boxplots: 25th to 75th percentiles, median, 1.5×interquartile as whiskers. (**e**) Representative images of HSF1-mCh (4 μM) with the 8 μM HSP40 and HSP90 in vitro. Scale bars, 2 μm. Images are representative of 3 independent experiments.

nature research

Corresponding author(s): Yujie Sun

Last updated by author(s): Dec 26, 2021

Reporting Summary

Nature Research wishes to improve the reproducibility of the work that we publish. This form provides structure for consistency and transparency in reporting. For further information on Nature Research policies, see our Editorial Policies and the Editorial Policy Checklist.

Statistics

For all statistical analyses, confirm that the following items are present in the figure legend, table legend, main text, or Methods section.

n/a	Confirmed
☐	☒ The exact sample size (*n*) for each experimental group/condition, given as a discrete number and unit of measurement
☐	☒ A statement on whether measurements were taken from distinct samples or whether the same sample was measured repeatedly
☐	☒ The statistical test(s) used AND whether they are one- or two-sided *Only common tests should be described solely by name; describe more complex techniques in the Methods section.*
☒	☐ A description of all covariates tested
☒	☐ A description of any assumptions or corrections, such as tests of normality and adjustment for multiple comparisons
☐	☒ A full description of the statistical parameters including central tendency (e.g. means) or other basic estimates (e.g. regression coefficient) AND variation (e.g. standard deviation) or associated estimates of uncertainty (e.g. confidence intervals)
☐	☒ For null hypothesis testing, the test statistic (e.g. *F*, *t*, *r*) with confidence intervals, effect sizes, degrees of freedom and *P* value noted *Give P values as exact values whenever suitable.*
☒	☐ For Bayesian analysis, information on the choice of priors and Markov chain Monte Carlo settings
☒	☐ For hierarchical and complex designs, identification of the appropriate level for tests and full reporting of outcomes
☐	☒ Estimates of effect sizes (e.g. Cohen's *d*, Pearson's *r*), indicating how they were calculated

Our web collection on statistics for biologists contains articles on many of the points above.

Software and code

Policy information about availability of computer code

Data collection	All the Live cell data, super resolution data and single molecule imaging data are collected on a custom Olympus IX83 inverted microscope equipped with a 100X UPlanSApo, N.A. = 1.49, oil-immersion phase objective and Andor iXon Ultra EMCCD. All the in vitro data and FRAP data are collected using Zeiss LSM 880 confocal microscope. The Gal4-mClover reporter assay was performed using the CytoFLEX Flow Cytometer. The western blot was performed on Bio-Rad ChemiDoc XRS. The EMSA was performed on FUJI LAS-4000 fluorescence imager (Fuji 800 Photo Film, Dusseldorf, Germany). The qPCR experiment was performed on Quantagene q225.

Data analysis	Raw DIC and fluorescent images were processed using ZEN (Zeiss,ver 4.10.0),Fiji (National Institutes of Health),Imaris (Oxford Instruments, ver 9.01) software for display. Fiji was used for droplet number and partition ration analysis. The Imaris (Oxford Instruments) software was also used for co-localization analysis in the super resolution imaging. All the analysis results were merged and plotted using RStudio with custom codes and script. For the analysis of super resolution image, custom MATLAB (2021a) code was used (All custom code used in this study is available upon request). FlowJo (ver 10.5.3) software was used for the analysis of flow cytometry data. For Cut&Tag data analysis, Subread (ver 2.0.3)-align was used for align of the paired-end reads to human genome build GRCh38/hg18 . The SEACR (ver 1.3) was used for peak identification . Homer (ver 4.10.0) 'annotatePeaks' and 'find-MotifsGenome' functions were used to annotate the called peaks and to find enriched motifs in these called peaks . DeepTools (ver 2.0) was used for transformation of bam file into read coverage files (bigwig format). 'bamCompare' functions of DeepTools was used for the generation of Genomic binding profiles. 'computeMatrix' and 'plotHeatmap' functions of DeepTools were used for the generation of Heat maps for ChIP-seq signals. Integrative Genome Viewer (IGV, ver 2.11.0) was used for visualization of Cut&Tag peaks. The iDEP web tool (ver .94) was used to adjust RNA seq read counts. The DESeq2 package (ver 1.34.0) was used for differential expression analysis of RNA seq data.

For manuscripts utilizing custom algorithms or software that are central to the research but not yet described in published literature, software must be made available to editors and reviewers. We strongly encourage code deposition in a community repository (e.g. GitHub). See the Nature Research guidelines for submitting code & software for further information.

Data

Policy information about availability of data

All manuscripts must include a data availability statement. This statement should provide the following information, where applicable:

- Accession codes, unique identifiers, or web links for publicly available datasets
- A list of figures that have associated raw data
- A description of any restrictions on data availability

All the data that are associated with the figures are provided as supplementary data. Human genome GRCh38/hg18 was used for the alignment of Cut&Tag and RNA-seq dataset. Cut&Tag and RNA-seq Datasets generated in this study have been deposited to NCBI GEO under the accession number GSE192370 and GSE191134.

Field-specific reporting

Please select the one below that is the best fit for your research. If you are not sure, read the appropriate sections before making your selection.

☒ Life sciences ☐ Behavioural & social sciences ☐ Ecological, evolutionary & environmental sciences

For a reference copy of the document with all sections, see nature.com/documents/nr-reporting-summary-flat.pdf

Life sciences study design

All studies must disclose on these points even when the disclosure is negative.

Sample size	For single molecule and super resolution imaging, more than 10 cells were used in each group. For conventional imaging, more than 100 cells were analyzed in each group. Each of the in vitro experiment was repeated 2-3 times. During each repeat, more than 10 fields of view were collected for further analysis. For qPCR assay, four independent wells were used for each target gene. For mClover reporter assay, 5 independent wells were collected for each HSF1 mutant and truncations. We determined the sample sizes based on previous publications and our experience. The sample size is sufficient since we usually detect large difference between two experimental conditions, with p-value lower than 0.01.
Data exclusions	No data were excluded in the samples.
Replication	Each experiment was repeated 2-3 times. All attempts at replication are successful.
Randomization	Not relevant to the study, as this study does not involve randomization of samples/organisms/participants.
Blinding	This study does not require investigators to be blinded to group allocation during data collection and/or analysis, as they were quantitative comparisons as determined by software or measurements.

Reporting for specific materials, systems and methods

We require information from authors about some types of materials, experimental systems and methods used in many studies. Here, indicate whether each material, system or method listed is relevant to your study. If you are not sure if a list item applies to your research, read the appropriate section before selecting a response.

Materials & experimental systems

n/a	Involved in the study
☐	☒ Antibodies
☐	☒ Eukaryotic cell lines
☒	☐ Palaeontology and archaeology
☒	☐ Animals and other organisms
☒	☐ Human research participants
☒	☐ Clinical data
☒	☐ Dual use research of concern

Methods

n/a	Involved in the study
☐	☒ ChIP-seq
☐	☒ Flow cytometry
☒	☐ MRI-based neuroimaging

Antibodies

Antibodies used

HSF1 primary antibodies (CST, D3L8I, Rabbit mAb #12972), Goat anti-Mouse IgG(H+L) Secondary Antibody-Alexa Fluor 647/ Cy3B((ThermoFisher, A-21240), Rabbit IgG (H+L) Cross-Adsorbed Secondary Antibody-Alexa Fluor 647/Cy3B (ThermoFisher, A-21244), GAPDH Mouse Monoclonal (1E6D9, Proteintech, #60004-1-Ig), Recombinant Anti-Brd4 antibody [EPR5150(2)] (abcam, ab128874),Recombinant Anti-Cyclin T1 antibody [EPR17982] (abcam,ab184703),Recombinant Anti-RNA polymerase II CTD repeat YSPTSPS (phospho S5) antibody [EPR19015] (abcam, ab193467),Recombinant Anti-RNA polymerase II CTD repeat YSPTSPS (phospho S2) antibody [EPR18855-87] - ChIP Grade (abcam, ab238146), Anti-Histone H3 (tri methyl K9) antibody - ChIP Grade (abcam, ab8898), Anti-Histone H3 (tri methyl K4) antibody - ChIP Grade (abcam, ab8580), Goat Anti-Rabbit IgG H&L (HRP) preadsorbed (abcam, ab7090), Goat Anti-Mouse IgG H&L (HRP) preadsorbed (abcam, ab97040), G3BP1 (CST, E9G1M, Rabbit mAb #61559), anti-HA-Tag (C29F4, Rabbit mAb #3724), Guinea Pig anti-Rabbit IgG (Heavy & Light Chain) antibody (Antibodies-Online ABIN101961).

Validation

All antibodies used in this study were commercial. Validation of the species and application of all the antibodies we used were described and can been found in the manufacturers' websites and in previous publications listed on the websites.

Eukaryotic cell lines

Policy information about cell lines

Cell line source(s)

HeLa S6, HEK293T, A549, MDA-MB-231, U2OS cells were purchased from ATCC. HEK293F cells purchased from ThermoFisher.

Authentication

None of the cell lines were authenticated within 1 year.

Mycoplasma contamination

All cell lines were tested negative for mycoplasma contamination.

Commonly misidentified lines
(See ICLAC register)

No misidentified cell lines.

ChIP-seq

Data deposition

☒ Confirm that both raw and final processed data have been deposited in a public database such as GEO.

☒ Confirm that you have deposited or provided access to graph files (e.g. BED files) for the called peaks.

Data access links
May remain private before publication.

https://www.ncbi.nlm.nih.gov/geo/query/acc.cgi?acc=GSE192370

Files in database submission

GSM5745738 BRD4-HS-Rep1
GSM5745739 BRD4-HS-Rep2
GSM5745740 BRD4-NHS-Rep1
GSM5745741 BRD4-NHS-Rep2
GSM5745742 CYCT1-HS-Rep1
GSM5745743 CYCT1-HS-Rep2
GSM5745744 CYCT1-NHS-Rep1
GSM5745745 CYCT1-NHS-Rep2
GSM5745746 M1-NHS-Hex-Rep1
GSM5745747 M1-NHS-Hex-Rep2
GSM5745748 M1-NHS-Rep1
GSM5745749 M1-NHS-Rep2
GSM5745750 M3-HS_Rep1
GSM5745751 M3-HS_Rep2
GSM5745752 M3-NHS_Rep1
GSM5745753 M3-NHS_Rep2
GSM5745754 Pol_II-HS-Rep1

GSM5745755 Pol_II-HS-Rep2
GSM5745756 Pol_II-NHS-Rep1
GSM5745757 Pol_II-NHS-Rep2
GSM5745758 WT-HS-Hex-Rep1
GSM5745759 WT-HS-Hex-Rep2
GSM5745760 WT-HS-Rep1
GSM5745761 WT-HS-Rep2
GSM5745762 WT-NHS-Rep1
GSM5745763 WT-NHS-Rep2

Genome browser session
(e.g. UCSC)

We used integrative Genome Viewer (IGV, ver 2.11.0) to display the ChIP-seq Tracks.

Methodology

Replicates

26 samples are sequenced, each with 2 replicates.

Sequencing depth

M1-HS-Hex-Rep1: Total fragments : 13,514,811 Mapped : 11,495,656 (85.1%)
M1-HS-Hex-Rep2:Total fragments : 11,700,390, Mapped : 10,028,403 (85.7%)
M1-NHS-Rep1:Total fragments : 4,866,297,Mapped : 3,168,323 (65.1%)
M1-NHS-Rep2: Total fragments : 3,916,072,Mapped : 2,480,066 (63.3%)
M3-HS_Rep1:Total fragments : 5,124,543,Mapped : 4,004,313 (78.1%)
M3-HS_Rep2:Total fragments : 4,487,958, Mapped : 3,509,825 (78.2%)
M3-NHS_Rep1:Total fragments : 25,881,614, Mapped : 16,813,436 (65.0%)
M3-NHS_Rep2:Total fragments : 15,149,501,Mapped : 10,540,468 (69.6%)
WT-HS_Rep1:Total fragments : 23,764,885,Mapped : 19,782,939 (83.2%)
WT-HS-Hex-Rep1: Total fragments : 13,494,556, Mapped : 11,406,463 (84.5%)
WT-HS-Hex-Rep2:Total fragments : 13,835,104, Mapped : 11,744,292 (84.9%)
WT-HS-Rep2: Total fragments : 13,048,827, Mapped : 10,837,559 (83.1%)
WT-NHS-Rep1:Total fragments : 981,764, Mapped : 577,826 (58.9%)
WT-NHS-Rep2:Total fragments : 787,719 , Mapped : 510,741 (64.8%)
BRD4-HS-Rep1:Total fragments : 20,893,130, Mapped : 17,752,535 (85.0%)
BRD4-HS-Rep2:Total fragments : 6,333,898, Mapped : 5,383,576 (85.0%)
BRD4-NHS-Rep1:Total fragments : 6,086,285, Mapped : 5,178,084 (85.1%)
BRD4-NHS-Rep2:Total fragments : 4,816,416, Mapped : 4,110,665 (85.3%)
CYCT1-HS-Rep1: Total fragments : 17,100,744, Mapped : 14,056,816 (82.2%)
CYCT1-HS-Rep2: Total fragments : 13,427,274,Mapped : 11,032,910 (82.2%)
CYCT1-NHS-Rep1:Total fragments : 5,514,919, Mapped : 4,258,991 (77.2%)
CYCT1-NHS-Rep2:Total fragments : 3,162,841, Mapped : 2,443,270 (77.2%)
Pol_II-HS-Rep1: Total fragments : 8,370,581, Mapped : 7,255,610 (86.7%)
Pol_II-HS-Rep2: Total fragments : 7,641,358, Mapped : 6,658,776 (87.1%)
Pol_II-NHS-Rep1: Total fragments : 13,867,384, Mapped : 11,807,922 (85.1%)
Pol_II-NHS-Rep2: Total fragments : 11,284,129, Mapped : 9,814,745 (87.0%)

Antibodies

HSF1 primary antibodies (CST, D3L8I, Rabbit mAb #12972), Recombinant Anti-Brd4 antibody [EPR5150(2)] (abcam, ab128874),Recombinant Anti-Cyclin T1 antibody [EPR17982] (abcam,ab184703),Recombinant Anti-RNA polymerase II CTD repeat YSPTSPS (phospho S5) antibody [EPR19015] (abcam, ab193467),Recombinant Anti-RNA polymerase II CTD repeat YSPTSPS (phospho S2) antibody [EPR18855-87] - ChIP Grade (abcam, ab238146), Guinea Pig anti-Rabbit IgG (Heavy & Light Chain) antibody (Antibodies-Online ABIN101961)

Peak calling parameters

The SEACR software was used for peak identification with data from IgG1 input as controls

Data quality

FastQC was run on all samples to ensure data quality.

Software

For Cut&Tag data analysis, the paired-end reads were aligned to human genome build GRCh38/hg18 using Subread-align. The SEACR software was used for peak identification with data from IgG1 input as controls and default parameters. Homer (ver 4.10.0) 'annotatePeaks' and 'find-MotifsGenome' functions were used to annotate the called peaks and to find enriched motifs in these called peaks. Alignment files in the bam format were also transformed into read coverage files (bigwig format) using DeepTools 60 for visualization in the Integrative Genome Viewer (IGV). Genomic binding profiles were generated using the deepTools 'bamCompare' functions. Heat maps for ChIP-seq signals were generated using the deepTools 'computeMatrix' and 'plotHeatmap' functions.

Flow Cytometry

Plots

Confirm that:

☒ The axis labels state the marker and fluorochrome used (e.g. CD4-FITC).

☒ The axis scales are clearly visible. Include numbers along axes only for bottom left plot of group (a 'group' is an analysis of identical markers).

☒ All plots are contour plots with outliers or pseudocolor plots.

☒ A numerical value for number of cells or percentage (with statistics) is provided.

Methodology

Sample preparation	Control or transfected HeLa S6 cells were washed with 1× PBS for 3 times and collected in 0.25% trypsin for 2 mins, spun down for 3 mins at 500 g and resuspended in 1× PBS. Flow cytometry was performed on CytoFLEX Flow Cytometer. Cells were gated for viability and single cells. All the parameters remained constant within parallel experimental runs for comparation.
Instrument	the CytoFLEX Flow Cytometer.
Software	All flow cytometry data were analyzed with FlowJo.
Cell population abundance	Populations in this study were composed of cancer cell line HeLa S6 with 9XUAS-mClover3 stable insertion into the genome exclusively. These cells were expanded form a single cell clone and very pure. No other cell population was used in this study. About 10000 cells of HeLa S6 with 9XUAS-mClover3 stable insertion into the genome were collected in each independent experiment. The analyzed populations were double positive for mClover3 and mScarlet, ranging from 5% to 30% in total cell population.
Gating strategy	Forward scatter (FSC) versus side scatter (SSC) gating were used for the selection of cells of interest and exlcude debris and dead cells. Cell aggregates were also exclude to select only single cells. Untransfected cells were used as negative control.

☒ Tick this box to confirm that a figure exemplifying the gating strategy is provided in the Supplementary Information.